
Article:
Zhao, X, Qi, K, Patacci, M orcid.org/0000-0003-1675-4643 et al. (2 more authors) (2019) Submarine channel network evolution above an extensive mass-transport complex: A 3D seismic case study from the Niger delta continental slope. Marine and Petroleum Geology, 104. pp. 231-248. ISSN 0264-8172

https://doi.org/10.1016/j.marpetgeo.2019.03.029

Accepted Manuscript

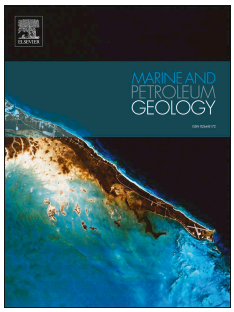

Submarine channel network evolution above an extensive mass-transport complex: A 3D seismic case study from the Niger delta continental slope

Xiaoming Zhao, Kun Qi, Marco Patacci, Chengpeng Tan, Tao Xie

PII: S0264-8172(19)30128-X

DOI: https://doi.org/10.1016/j.marpetgeo.2019.03.029

Reference: JMPG 3770

To appear in: *Marine and Petroleum Geology*

Received Date: 21 November 2018

Revised Date: 16 March 2019

Accepted Date: 22 March 2019

Please cite this article as: Zhao, X., Qi, K., Patacci, M., Tan, C., Xie, T., Submarine channel network evolution above an extensive mass-transport complex: A 3D seismic case study from the Niger delta continental slope, *Marine and Petroleum Geology* (2019), doi: https://doi.org/10.1016/j.marpetgeo.2019.03.029.

Title

Submarine channel network evolution above an extensive mass-transport complex: a 3D seismic case study from the Niger Delta continental slope

Authors

Xiaoming Zhao[a,b], Kun Qi [a,b*], Marco Patacci[c], Chengpeng Tan[a,b], Tao Xie[a,b]

a Key Laboratory of Natural Gas Geology of Sichuan Province, Sichuan 610500, China

b School of Geoscience and Technology, Southwest Petroleum University, Sichuan 610500, China

c Turbidites Research Group, School of Earth & Environment, University of Leeds, Leeds LS2 9JT, United Kingdom

Contact information

Abstract:

A submarine channel network, named Abalama Channel System (ACS), has been recognised in the subsurface of the Niger Delta continental slope. It overlies a mass-transport complex (MTC) and consists of six channel segments, delimited by five avulsion points and one confluence point. High-resolution 3D seismic data are used to investigate the development of the ACS and to describe the interaction between the channels and the underlying MTC. The MTC mainly consists of highly disaggregated materials (MTC matrixes) and in plan-view has a very complex fingered geometry, characterised by the presence of erosional remnants (remnant blocks). The different character of the MTC matrixes compared to that of the remnant blocks likely resulted in a bathymetry characterised by negative and positive relief, which provided the initial confinement for the channels of the ACS. In areas where the MTC-induced confinement was weak or decreased abruptly, channels tended to develop higher sinuosity, increasing channels instability and ultimately causing avulsions. Three ideal categories of submarine channel avulsions are observed. Type 1 is characterised by parent and avulsion channel having similar size and maturity; Type 2 is characterised by a large, high-maturity parent channel and a small, low-maturity avulsion channel; Type 3 emphasizes the larger scale and higher maturity of the avulsion channel compared to the parent channel. In the distal part of the study area, topography related to mud diapirs provided lateral confinement that captured flows avulsed at different times resulting in a channel confluence phenomenon. Submarine channel network evolution recorded by avulsion and confluence points represents an important research theme in deep-water sedimentology, as it controls the final distribution of sediments and the extension of sands in the whole deep-water depositional system; hence this study can be used to guide hydrocarbon exploration in analogue systems.

Keywords: Submarine channel network; Avulsion; Confluence; Mass-transport complex; Niger Delta slope

1. Introduction

Submarine channel networks have developed in many deep-water systems (Amazon Fan, Pirmez et al., 1997; Zaire Fan, Droz et al., 2003; Indus Fan, Kenyon et al., 1995; Bengal Fan, Curray et al., 2003) as a direct result of frequent submarine channel (including canyons, fan valleys and even distributaries) avulsion events (Damuth et al., 1983a; b; Kolla and Coumes, 1987; Manley and Flood, 1988; Flood et al., 1991) and the occasional confluence phenomenons (e.g., Curray et al., 2003; Fildani et al., 2013; Maier et al., 2013). These networks of channels play an essential role in determining the sediment dispersal pattern and the growth of the whole fan (Piper and Normark, 1983; Manley and Flood, 1988; Primez and flood, 1995; Ortiz-Karpf et al., 2015) and therefore are with great research value and meaning in the hydrocarbon industry.

Mass-transport deposits (MTDs) or complexes (MTCs), sets of strata specifically generated in submarine instability events (Moscardelli et al., 2006; Bull et al., 2009; Alves, 2015), can extensively modify seafloor morphology, generate localised accommodation space, and ultimately change the drainage architectures on the continental slope to influence the submarine sediment routing (Joanne et al., 2010; Olafiranye et al., 2013; Kneller et al., 2016; Ward et al., 2018). In some extreme cases, they can even control the submarine channel avulsion or confluence; for example, Ortiz-Karpf et al. (2015) introduced the role of mass-transport complexes in triggering the occurrence of channel avulsion and controlling the evolution of subsequent avulsion channels/lobes in Magdalena Fan, offshore Colombia. Qin et al. (2017), on the other hand, investigated the effect of mass-transport deposits in terms of capturing unconfined flows to merge distinct channels offshore Espirito Santo Basin, SE

Brazil. However, those works only concentrated on an individual avulsion or confluence event. The evolution of a complete and independent submarine channel network, with both avulsion and confluence events and overlying on an extensive mass-transport complex, has never been studied.

The present study focuses on the evolution of a channel network in the subsurface of the Niger Delta continental slope, informally named the 'Ablama Channel System' (abbreviated as ACS), which overlies a large-scale mass-transport complex. The ACS consists of six channel segments, connected by five avulsion points (abbreviated as AP) and one confluence point (abbreviated as CP). Utilizing high-resolution seismic data, we (1) investigate the emplacement of a 120 km^2 MTC and its effect on the overlying channels, (2) characterise the avulsion points using a more quantitative approach and summarised their basic types, and (3) analyse the significance of a channel confluence point, which occurred in the downstream reach. These new insights can be applied to hydrocarbon exploration in analogue deep-water deposits.

2. Geological setting

The study area is defined by a 225 km^2 3D seismic volume located in the subsurface of the Niger Delta continental slope along the South Atlantic margin, with a water depth ranging from 1300 to 1700 m (Fig. 1A). The sediment is sourced from a large regressive delta, the Niger Delta, with an area of 12×10^4 km^2 (Doust and Omatsola, 1989). Under the gravity-driven tectonics, the Niger Delta sedimentary packages slips basinward, resulting in three sectors characterised by different tectonic regimes (Doust and Omatsola, 1989; Damuth, 1994; Morley and Guerin, 1996). These are an upper extensional zone, extending from the onshore to the outer shelf and characterised by listric normal faults, a translational zone, located on the upper continental slope and dominated by mud diapirs, and a lower compressional zone,

spanning the lower slope as well as the continental rise and including a series of linear toe thrusts (Damuth, 1994) (Fig. 1B). The study area is located in the most basinward part of the transitional zone (Fig. 1B).

Three main sedimentary successions were developed in the Niger Delta Basin during the Cenozoic; in chronological order (from older to younger) they are the Akata, Agbada and Benin Formations (Short and Stäuble, 1967) (Fig. 1B). The precise age of the study interval is uncertain, but it is inferred to be part of the Agbada Formation, because of its shallow burial depth (less than 300 m) and the specific geographical location of the study interval (Fig. 1B). Also, according to the similar geographical location and water and burial depths of the study interval to the study subject of Deptuck et al. (2007), its time interval should roughly be less than 2 Ma.

3. Methodology

3.1 Dataset

The primary dataset used in this work is a 3D seismic volume extending over an area of 225 km^2, acquired by China National Offshore Oil Corporation (CNOOC). All seismic-reflection data were processed to zero phase and displayed in SEG reversed polarity, such that an increase in acoustic impedance corresponds to a high-amplitude trough (negative) reflection. The data have a sample rate of 3 ms and a bin size of 12.5 m×12.5 m. The seismic frequency bandwidth is 15 – 90 Hz, with a dominant frequency of approximately 70 Hz in the study interval. Depth conversions are made assuming a seismic velocity of 1480 m/s for seawater and 1900 m/s for shallow sediments (Liu et al., 2013), yielding a vertical resolution of approximately 6 m, which enables the target channels of this study to be well characterised.

3.2 Seismic analysis

This study is principally based on 'classical' 2D seismic facies analysis (Vail et al., 1977), combined with a 3D seismic geomorphology approach (Posamentier et al., 2007). Seismic facies analysis was based on the continuity, amplitude, cross-sectional geometry and termination of seismic reflections. In seismic profiles located around the avulsion points, cross-cutting and onlapping relationships of reflectors belonging to channel fills and levee deposits of different channels can help us to determine the relative timing of avulsion events, which will be clarified in detail later in the paper. The 3D seismic geomorphology approach enabled enhanced visualization of seismic facies distribution in map view through coherence and root mean square amplitude extractions. In addition, two-way traveltime (TWT) structural maps of channel floors were made around each avulsion point to help understand the avulsion events and their chronological sequence.

It is important to note that due to the absence of lithological calibration from wells, the interpretations of seismic facies as specific sedimentary packages was based on the comparison with published seismic-based studies on deep-water sedimentology (Table 1).

3.3 Channel dimensions and morphology

Dimensional and morphological parameters, including widths, heights, cross-sectional areas and sinuosities have been used, following common practice on quantitative descriptors of submarine channels (see Catterall et al., 2010; Mulder et al., 2012; Qin et al., 2017). In the present study, quantitative analyses were conducted along the main pathways of six channels, with their widths, heights and cross-sectional areas measured at 62.5 m intervals; due to levees are not uniformly developed in all these channels, for simplifying sake, such morphometrics take no account of the presence or absence of levees and refer to the maximum value of these three parameters (Fig. 2A). Furthermore, only one sinuosity value

was calculated for each channel, representing the ratio of the along-channel length to the straight-line distance between its end-points (Fig. 2B).

4. Results

4.1 Seismic stratigraphy and seismic facies

4.1.1 Stratigraphic architecture

Four regional surfaces, namely from the top to the bottom T0 (present-day seafloor), T110, T130 and T200, could be traced in the shallow subsurface of the study area (Figs. 3A and 4A). The top interval between the seafloor (T0) and T110 has a thickness of 80-100 m and is characterised by low-amplitude, high-continuity reflections (Figs. 3A and 4A), presumably representing hemipelagic sediments. T110 and T130 act as the top and bottom boundaries of the study interval, which has a thickness of 185-200 m and various seismic reflection characteristics (Figs. 3B and 4B). The bottom interval bounded by T200 and T130 has a similar seismic expression to the top succession, but a rather smaller thickness of 15-20 m (Figs. 3A and 4A); it can be interpreted to represent a condensed section occurred during a sea level highstand.

4.1.2 Seismic facies and corresponding depositional elements

Five major seismic facies were identified in the study interval (Figs. 3B and 4B). They are interpreted as representing different depositional elements, according to recognition criteria based on published seismic-reflection datasets (Table 1).

Seismic facies 1 is characterised by variable-amplitude, discontinuous reflectors confined within a U- or V-shaped erosional surface and it is interpreted as submarine channel fill deposits (Abreu et al., 2003; Posamentier and Kolla, 2003; Gee et al., 2007). Facies 2, usually found on either side of facies 1 strata, is composed of low-amplitude, continuous

reflectors that form wedge-shaped packages and is interpreted as external (master) levee deposits (Deptuck et al., 2003; Nakajima and Kneller, 2013; Zhao et al., 2018a). Facies 3 consists of variable-amplitude, chaotic reflection packages and is considered to represent MTC (Gong et al., 2014; Ortiz-Karpf et al., 2015). Moreover, Bull et al. (2009) and Gamboa et al. (2011) called such deposits as "MTC debrites/matrixes". Facies 4 is characterised by parallel, high amplitude, continuous reflectors and is generally interpreted as indicating lobe deposits (Weimer and Slatt, 2007; Saller and Dharmasamadhi, 2012). Facies 5 shows variable-amplitude, continuous reflections packages with irregular external geometry. These packages appear truncated and surrounded by the Facies 3 (MTC matrixes) and thus they are interpreted as remnants of a stratigraphic interval otherwise mostly eroded by mass flows (Posamentier, 2004; Moscardelli et al., 2006; Bull et al., 2009; Ortiz-Karpf et al., 2015). Gamboa et al. (2011) and Ward et al. (2018), however, named these erosional remnants as "remnant blocks of strata", different from the "rafted blocks" that are substantially translated during mass-wasting process, commonly embedded in MTC matrixes and present significant disruption of basal strata. Those remnant blocks are left in situ and are totally cohesive with the strata at their base. In addition, for the early stratigraphic interval, complete strata preservation is observed in the eastern-most and western-most parts of the study area near the lateral scarps of the large MTC (eastern scarp, Fig. 3B and western scarp, Fig. 4B).

The top surface of the MTC was locally incised into by subsequent submarine channels and the resulting stratigraphy was onlapped by lobes that were deposited in the underfilled erosional depressions of MTC and submarine channels (Figs. 3B and 4B).

4.2 MTC: the substrate of channel development

4.2.1 General description of the MTC

184 The studied MTC is composed of seismic facies 3 (with facies 5 representing remnant
185 blocks), covering an area of approximately 120 km^2 (Fig. 5). Its basal surface is highly
186 erosional, truncating pre-existing strata and resulting in many erosional troughs. The depth of
187 these erosional depressions is variable, ranging from 70 to 105 m, showing a downslope
188 decreasing trend (Fig. 6).

189 The studied MTC has a lobe-like shape, and it is overall elongated in a downslope
190 direction (Figs. 5 and 7). In the northernmost part, the basal surface of the MTC shows a U-
191 shaped morphology, implying a confined setting; however it looks that relatively close in the
192 downstream direction the mass flows spread out southward (Figs. 7A and 7B). In the
193 southernmost part, where mud diapirs developed, the MTC was confined by bathymetric
194 highs and was deflected by them (Figs. 4 and 5A). This is shown by a change in the general
195 elongation of the MTC from N-S to NE-SE in the southern extent of the study area (Fig. 7A).
196
197 4.2.2 Component elements and the irregular top surface of the MTC
198 In addition to the seismic expression in cross sections (see Table 1), the MTC matrixes
199 (Facies 3) can be recognised thanks to a dark-colored coherent pattern (Figs. 5A and 7A).
200 This facies infills the erosional troughs at the base of the MTC and it has a total area of
201 approximately 80 km^2 and a thickness of 62-93 m. Its thickness is smaller than the depth of
202 the erosional troughs (Figs. 3B and 4B), suggesting that the MTC matrixes did not totally fill
203 the erosional troughs. This must have resulted in negative relief left prior to the development
204 of submarine channels (Fig. 7A).
205 The remnant blocks (facies 5) represent the other significant component in the area of
206 the MTC. They commonly show narrow ‘ridge’ geometries in cross sections (Figs. 3B and
207 4B) and irregular shapes in map-view (Figs. 5A and 7A), with a total area of around 40 km^2.
208 Their main axes are diverging from each other and they can be traced back to a point in the

proximal domain of the study area, which seems to represent the location where the mass-transport complex becomes spread (Fig. 7A). In addition, these preserved remnants of the older seafloor are higher than the top surface of the deposited MTC matrixes (Figs. 3B and 4B) and therefore must have formed positive bathymetric anomalies, present at the onset of channel network development (Fig. 7A).

4.3 'Ablama Channel System' (ACS)

4.3.1 General description

In the study area, the 'Ablama Channel System' (ACS) consists of six channels, named C1a, C1b, C1c, C2a, C2b and C2c (from the oldest to the youngest) (Fig. 5). All of them were initiated by avulsion events that occurred somewhere along the length of the parent channel (the established one whose flow is diverted). Five avulsion points can be recognised, named AP1 through AP5 (Fig. 5). These channels have an apparent distributary pattern upslope where C1b and C2b have diverged from the confined area of the MTC trending parallel to the lateral scarps, and a tributary pattern downslope where the younger C2a have reoccupied the older C1b, giving the appearance of a channel merger or confluence (Figs. 5 and 6).

These channels developed above the MTC matrixes and were confined by the positive-relief remnant blocks and by the MTC's lateral scarps (Figs. 5 and 6). In some cases, these channels are juxtaposed directly against the remnant blocks (e.g., channel C2b in Fig. 6A). Furthermore, each avulsion point originates from a bend of the parent channel (Figs. 5, 8 and 9), though in some cases this configuration may be damaged and obscured by the continued development of the younger avulsion channel (Figs. 9A and 9B); for example, at AP4 that bend of C2a is hardly recognised (Figures 5B and 9B). The vertexes of these bends are adjacent to the heads of the avulsion channels, implying that the avulsion events preferentially occurred on the outside of a sharp bend of the parent channel (Figs. 8 and 9).

234

235 4.3.2 Channels of the ACS

236 The oldest channel documented in this study is C1a; it trends to the southeast, shows a
237 sinuosity of 1.12 and lacks observed levee deposits (Fig. 5 and Table 2). Its widths, heights
238 and cross-sectional areas at different locations in the study area vary slightly, with the
239 amplitudes of 62 m, 14 m and 4601 m^2 respectively. (Fig. 10 and Table 2). C1b, bounded by
240 levee packages in the upstream reach, avulsed from C1a and initially took a course to the
241 south before turning southwest, resulting in a higher sinuosity of 1.21 (Figs. 5 and 8A, Table
242 2). The widths, heights and cross-sectional areas of C1b vary significantly along its length,
243 with the amplitudes of 403 m, 55 m, and 27887 m^2 respectively, and uniformly show a
244 clearly decreasing trend downstream. Furthermore, around the two avulsion points (AP1 and
245 AP2) it has flowed through, that decrease of scale parameters is extraordinarily marked (Figs.
246 5B and 10, Table 2). C1c avulsed from and developed on the right levee of C1b and headed
247 in a southerly direction with a very small sinuosity of 1.04 (Figs. 5 and 8B, Table 1). It has no
248 observed overbank deposits and it is the smallest channel in the study area, with the widths,
249 heights and cross-sectional areas of 123-180 m, 24-44 m and 1900-6234 m^2 respectively
250 (Figs. 8B and 10, Table 2).

251 C2a also avulsed from the right levee of C1b; however, its proximal reach (i.e. the
252 portion up-dip of AP4) has long been modified by the subsequent C2b and inherited the
253 general characteristics of it. Therefore, the proximal reach of C2a is better considered as part
254 of C2b (Figs. 5B and 9A). The C2a defined in the present study (Figs. 5B and 9B) lacks
255 observed levees and trends in a southwesterly direction to flow outside the study area (Table
256 2); it has a sinuosity of 1.09 and due to the abrupt morphological change around the
257 confluence point (Fig. 12), its dimensional parameters have relatively large ranges, with the
258 widths, heights and cross-sectional areas being 150-437 m, 32-72 m and 3117-14992 m^2

respectively (Table 2). C2b originated from C2a and it is also trending toward the southwest, with a sinuosity of 1.17 (Fig. 5 and Table 2); it is bounded by well-developed levees and has the largest size compared with the other channels, with the widths, heights and cross-sectional areas being 391-637 m, 58-108 m and 13656-38890 m^2 respectively (Table 2). Just like C1b, scale parameters of C2b also show a downstream decreasing trend and that decline could roughly be divided into two sections delimited by AP4; upstream the AP4, scale parameters decrease rapidly, however, downstream the AP4 they change slightly and almost show a flat trend (Fig. 11 and Table 2). As for C2c, it is a non-leveed channel with the relatively small widths, heights and cross-sectional areas of 110-212 m, 24-50 m and 2565-8460 m^2 respectively (Fig. 11 and Table 2); it avulsed from the left levee of the parent channel C2b and headed to the south before turning southwest (sinuosity of 1.08; Figs. 5 and 9C, Table 2).

4.3.3 Channel confluence

In the distal part of the study area, two mud diapirs developed and formed a bathymetric high prior or during the development of the ACS (Figs. 4 and 5A). For the east tributary C1b, that bathymetric high caused it to be diverted toward the southwest (Fig. 5B), resulting in a similar trend to the general orientation of the MTC in that area (Fig. 7A); for the west tributary C2a, it also reached the toe region of that bathymetric high and rejoined the abandoned C1b at the confluence point, hence creating a channel merger or convergence.

The part of C2a downstream of the CP shows much larger widths and cross-sectional areas than the parts of C1b and C2a upstream to it (Figs. 12A and 12C), however, the channel heights of the two tributaries don't change significantly across the confluence point (Fig. 12B).

5. Discussion

5.1 Origin and emplacement of the MTC

MTCs are generated as the result of a series of processes associated with sediments failures. They can be induced and ultimately triggered by a variety of processes alone or in combination, including increased sedimentation rate (Dugan and Stigall, 2010; Masson et al., 2010; Gong et al., 2014), eustatic sea-level changes (Manley and Flood, 1988; Brami et al., 2000; Masson et al., 2010), gas hydrate dissolution (Maslin et al., 2004; Grozic, 2010), and seismicity (Alfaro and Holz, 2014; Gong et al., 2014).

The overall extent of the studied MTC could not be mapped due to the limited area covered by the 3D seismic survey, but it seems most likely that it was not sourced from the proximal part of the study area because no headwall escarpment/scar, the symbol of the occurrence of mass wasting process (Moscardelli et al., 2006; Bull et al., 2009; Gamboa and Alves, 2016; Qin et al., 2017), could be recognised (Figs. 5A and 7A). Furthermore, considering the fact that in the northernmost part of the study area MTC appears confined within a U-shaped erosive morphology and in a short distance expanded out southward, forming an elongated lobe-shaped deposit (Figs. 5A and 7A), we put forward two speculations. Firstly, the studied MTC (located in a mid-slope position; see Fig. 1) is more likely to have originated from the failures of upslope regions, such as upper slope, shelf-margin or even the distal part of shelf-edge deltas though some MTCs oriented parallel to the continental slope do exist in some extreme cases (Ashabranner et al., 2010; Gamboa and Alves, 2016). These upslope failures may be associated with the rapid sedimentation rates and ‘escalator regression’ in the Niger Delta Basin since the Eocene (Doust and Omatsola, 1989; Cohen and McClay, 1996; Deptuck et al., 2007). Although constraining the absolute age of the mass-wasting event or events that deposited the studied MTC is impracticable due to the lack of chronological calibration, it is possible to observe that part of T130, the basal

boundary of the study interval, was used as the basal shear surface of the MTC (Figs. 3, 4 and 6). This suggests that T130 played a key role in delimiting the erosional depth of the MTC and that it is probably a mechanically weak layer acting as a detachment surface.

Secondly, mass flows responsible for the formation of the studied MTC most likely have exploited a pre-existing channel conduit to move downslope from the source area and deposited at the unconfined channel termination. When focusing along that pre-existing channel, mass flows tended to have high sediment delivery rate and in turn, they would entrench the deposited channel fills, damage the geometric channel forms, and ultimately give raise to the formation of basal grooves and rafted blocks embedded within highly-disaggregated debrites, which exactly concurs with the scenario within the proximal confined area of the studied MTC (Figs. 5A and 7B). Similar phenomena have also been observed offshore Trinidad (Moscardelli et al., 2006), offshore SE Brazil (Qin et al., 2017) and along the South China Sea margin (Gong et al., 2014), where basal grooves/linear striations and rafted blocks/megaclasts are also recognised in channel-confined MTCs. Further downstream, when lost the confinement of the early channel conduit those mass flows, on the contrary, tended to have relative low entrench rate for the substrate and hence resulted in the occurrence of large-volume remnant blocks (Figs. 5 B and 7A). At last, when mass flows encountering the bathymetric high imposed by mud diapirs, the emplacement direction of the MTC tended to be deflected toward the southwest, where many thrust-like feature are recognized (Fig. 7C). They could be caused by flow deceleration and internal contraction against bathymetric highs (Moscardelli et al., 2006; Ortiz-Karpf et al., 2017), a process which has been described from many deep-water basins around the world (Posamentier and Kolla, 2003; Moscardelli et al., 2006; Bull et al., 2009; Gong et al., 2014).

5.2 Role of MTC on channel evolution

The rugged seafloor caused by mass transport deposits have been documented in a number of studies based on outcrop analogues (Jackson and Johnson, 2009; Armitage et al., 2009), seismic data (Ortiz-Karpf et al., 2015; Kneller et al., 2016), well and core data (Eggenhuisen et al., 2010; Corella et al., 2016), and numerical models (Stright et al., 2013). In the study area, the target MTC is characterised by underfilled erosional scars and protruding remnant blocks, which respectively generated negative and positive reliefs on its upper surface (Figs. 3, 4, 6, and 7A), constituting the substrate for the development of later submarine channels. These bathymetric highs and lows acted as physiographic 'containers' for the turbidity flows responsible for the formation of the ACS. This resulted in the six studied channels occupying the same axial trends of the residual depressions and being confined at the largest scale within the bathymetric lows (Figs. 5 and 6). The channels used the underfilled erosional depressions as their preferential pathway, with the channel floors incised into the remobilised materials and never overriding the remnant blocks (Figs. 5 and 6). That spatial association between channels and remobilised materials could be explained by two primary factors. Firstly, the irregularities on the MTC top surface, as stated above, provided bathymetrical confinement to focus and channelize the turbidity flows. When the flow direction is oblique to a remnant block, turbidity flows do not seem to be able to spill over the obstacle, but they are diverted back toward the topographic depressions. Turbidity flows being diverted by topographic highs on MTD top surfaces have been suggested in other systems (Hansen et al., 2013; Masalimova et al., 2015; Corella et al., 2016; Ward et al., 2018). Secondly, differences in mechanical properties between disaggregated remobilised materials and remnant blocks caused different channel erosional capacity, resulting in increased erosion in the areas with remobilised material, therefore focusing the turbidity flows in those locations. As no significant thickness of background hemipelagic sediment can be identified in seismic sections between the MTC and the ACS (Figs. 3, 4, and 6), the time interval

between the emplacement of the MTC and the initiation of the channels seems to have been short. It is possible to speculate that the remobilised material did not have time to consolidate completely before the onset of the channels.

Although all the six documented channels are influenced by MTD-related topography, the type and degree of interaction varies between channels and along their studied length. In some places where channels were strongly confined by the remnant blocks, the avulsion channel (C1b) could directly use the block as the bank instead of aggradated levees. (Fig. 6A). In contrast, where the confinement was weak or decreased abruptly, channels tended to migrate laterally and develop meander bends (Fig. 5). Zhao et al. (2018b) described similar scenarios in the subsurface of the Niger Delta continental slope as well, where the up-dip segment of the Bukuma-minor channel has a sinuous course in the unconfined domain, but becomes straight where confined by a pre-existing channel-levee system. All the five avulsion events documented in the present study occurred on the outside of sharp bends in areas of relatively weak confinement (Figs. 5, 8 and 9). These sharp bends increase the local sinuosity leading to a more unstable channel course, which, when coupled with a triggering mechanism, can create the occurrence of an avulsion (Kolla, 2007). Avulsion occurring at the apex of a parent-channel sharp bend has been described in detail by Zhao et al. (2018a) and it is mainly associated with the flow stripping across the external levee and the resultant erosion. All in all, from aforementioned spatial association between channel distribution and MTC-related topography, it is suggested that mass wasting process and resultant MTCs can significantly change the drainage architecture and hence influence the sediment routing on continental slopes.

5.3 Basic types of submarine channel avulsion

After an erosional inception (Fildani et al., 2006; Kostic, 2011; Fildani et al., 2013), submarine channels tend to gradually develop levees and become more sinuous (Posamentier and Kolla, 2003; Gee et al., 2007; Maier et al., 2013). Such progressive evolution results from the cumulative impact of gravity flows that traversed a channel, shaping the channel morphology and, thus, reflects an increase of channel maturity (Maier et al., 2013). Using this definition of channel maturity, changes in sinuosity and levee development that occur as the parent channel 'transitions' into the avulsion one at the avulsion point can be interpreted as a result of difference in maturity of the avulsion channel with respect to its parent. According to such differences in maturity as well as to the variations in size (presented in Figs. 10 and 11) between the parent channel and avulsion channel, three end-members of submarine channel avulsion can be recognised (Fig. 13).

Type 1 is characterised by parent and avulsion channel having similar size and maturity (Fig. 13A). It is the most common and 'classical' avulsion event and has long been observed in deepwater settings (Kenyon et al., 1995; Primez et al., 1997; Curray et al., 2003). Towards the base of the avulsion channel, an avulsion lobe or splay usually occurs (Fig. 13A). Such sand-rich sheet deposits, formed at the start of an avulsion cycle, are seismically expressed as high-amplitude units that consist of relatively continuous to somewhat discontinuous reflections and are referred to as high amplitude reflection packets or HARPs (Flood et al., 1991; Primez et al., 1997). Considering the similarity of C1a, C1b and C2b around AP1 and AP3, as described in the results section (Figs. 8A, 9A, 10, 11 and Table 2), AP1 and AP3 are classified as avulsion type 1 (Table 3). However, no avulsion lobe is identified at the base of C1b or C2b. Drawing from the studies of HARPs by Prather (2000) and Posamentier and Kolla (2003), such absence of HARPs may be caused by the low gradient of C1a overbank slope or by the small sand-to-mud ratio of post-avulsion flows. During the initial phase of

avulsion these two factors might result in the establishment of a newly avulsed channel instead of an avulsion lobe or splay.

Type 2 is characterised by a large, high-maturity parent channel and a small, low maturity avulsion channel (Fig. 13B). This type represents an incomplete or aborted avulsion, and the associated avulsion channel was named by Zhao et al. (2018a) 'partially-avulsed channel', because of its small scale and failure to develop levees and high sinuosity (Fig. 13B). The preservation of such partial avulsion type relies on the abrupt stop of sediment supply to the avulsion channel, which in turn may be caused by the sudden shut-off of the whole deep-water system or by a successful and complete upstream avulsion of the parent channel (Fildani et al., 2006; Maier et al., 2013; Zhao et al., 2018a). Due to that sudden depositional quiescence of the avulsion channel, some characteristic signatures occurred prior to or in the initial period of avulsion process tend to be preserved, such as sediment waves and linear scours oriented perpendicular and parallel to the avulsed flows, respectively (Fig. 13B). Similar scenarios have also been described in a number of other systems such as: Monterey East System (Fildani and Normark, 2004; Fildani et al., 2006), Lucia Channel System offshore Central California (Fildani et al., 2013; Maier et al., 2013) and a channel-levee system on the Niger Delta continental margin (Armitage et al., 2012). This Type 2 scenario in the study area is recognised at AP2 and AP5 (Table 3), where C1c and C2c have much smaller scales and sinuosities than their parent channels and are not bounded by levees (Figs. 8B, 9C, 10, 11 and Table 2). It is worth noting that the scale parameters of C1c and C2c have some high-value anomalies along the depositional dip direction and in turn show a bell-shaped trend (Fig. 10), indicating they are incipient channels and therefore do not have continuous or smooth thalwegs. In addition, near AP2 and AP5 no sediment waves or linear scours could be identified, which may be explained by their small scales that could not be resolved with the available seismic resolution.

In contrast to Type 2, Type 3 emphasizes the larger scale and higher maturity of the avulsion channel compared to the parent channel (Fig. 13C). This means the avulsion channel has gone through a significant evolution after avulsion. Due to the long development, the avulsion channel has totally eroded the avulsion lobe around the avulsion point and its levee overlies the head of the parent channel (Fig. 13C). In the study area, this type of avulsion is observed at AP4 (Table 3), where the avulsion channel C2b has much larger dimensions and sinuosity than C2a and is bounded by well-developed levees that downlap upon the most upstream part of C2a (Figs. 9B, 11 and Table 2).

5.4 Channel confluence point

A turbidity current escaping channel confinement due to an initial avulsion will seek pathways along the highest gradient to reach the base level. In the southern part of the study area, at the toe region of a bathymetric high created by mud diapirs (Figs. 4 and 5), is located a confluence point (CP). In this region, a topographic low and the presence of lateral confinement provide favourable conditions to capture the flows derived from different avulsion events and finally gave rise to the appearance of channel confluence. When C1b was active, turbidity flows tended to be deflected into the confluence region due to the presence of mud diapirs (Fig. 5); such diverting of submarine channels associated with structural forcing has been documented in many case studies (Clark et al., 2009; Gamboa et al., 2012; Jolly et al, 2016; Zucker et al., 2017). When C2a was active, the early C1b channel may still be underfilled because its downstream segment had just been abandoned, which could reinforced the ability of the confluence region to capture flows and again captured the turbidity flows derived from AP3 where C2a avulsed from. Such submarine channel confluences occurring adjacent to salt diapirs have also been identified in the southeast Brazilian Margin (Gamboa et al., 2012; Qin et al., 2017).

Gamboa et al. (2012) proposed that submarine confluences can be classified as symmetric or asymmetric based on the equality of the angles the tributaries bear to the post-confluence channel. The confluence in the study area is characterised by a typical 'Y'-shaped junction (Figs. 5 and 12) where two tributaries have identical sizes (Fig. 12) and hence it is classified as symmetric. This type of junctions have been observed in modern submarine canyons by Mitchell (2004) and are also considered in the general models for river-based studies (Bathurst, 1997; Best and Roy, 1991; Wang et al., 1996). In addition, the predominance of widening process over channel incision around the confluence point (Fig. 12) indicate during C2b rejoining the C1b the interaction between MTD and turbidity flows responsible for the formation of C2b were dominated rather than the traditional cut-and-fill process within channels. Therefore, part of MTD was again removed downslope by C2b and replaced by channel-fill deposits. That MTD-turbidity flow interaction could be explained by the unconsolidated and friable MTD materials. MTD was weaker than the strata beneath T130, and, as a result, turbidity flows preferentially eroded the more friable MTD above T130, instead of incising downward into older deposits. This process resulted in a pronounced widening of the older channel with small change in its heights (Fig. 12).

5.5 Temporal-spatial evolution of the Abalama Channel System (ACS)

It has been suggested from studies of several deep-water fans that avulsion events result in the abandonment of parent channels down-dip of the avulsion sites, and that at any one time only one channel is largely active (Curray and Moore, 1971; Damuth et al., 1983a, b; Droz et al., 2003; Kolla, 2007). The same appears to be true for the ACS in the study area, i.e., the studied avulsion events and corresponding avulsion channels have occurred at different

481 times. Channels C1a, C1b, C1c, C2a, C2b and C2c were active sequentially, with C1a being
482 the oldest and C2c the youngest.

483 Based on the character and location of the avulsions, the channel network evolution can
484 be broadly divided into two phases: Phase I and Phase II (Fig. 14F). Phase I was
485 characterised by the avulsion points stepping landward (i.e. toward the shelf) with time (Fig.
486 14F). In Phase I, C1b appears to have avulsed from C1a at AP1(Fig. 14A), after which C1b
487 became an active channel and the parent channel C1a, down-dip of that avulsion, was
488 eventually abandoned (Fig. 8A). The up-dip portion of C1a, however, was still an active
489 conduit directly leading into C1b and hence worked as the upstream reach of it (Fig. 5A). As
490 a result, the upstream reach of C1b was the active conduits for a longer time than its
491 downstream counterpart, which can explain the observation that the dimensions of C1b
492 decrease downstream and show an apparent slump around the avulsion points (Figs. 10 and
493 14). Following this, an avulsion occurred at AP2 (Fig. 14B), up-dip of that of C1b, and led to
494 the creation of C1c that truncated the right levee of C1b (Fig. 8B). As stated above, the
495 avulsion of C1c belongs to Type 2, i.e., an aborted/incomplete avulsion (Table 3), and it is
496 most likely that it was because of the successful and complete upstream avulsion of C2a at
497 AP3 that sediment supply from C1b to C1c abruptly stopped. The avulsion of C2a at AP3
498 (Fig. 14C) represents the end of Phase I and the start of Phase II. Phase II is characterised by
499 avulsions successively stepping basinward and leading to the establishment of C2b and C2c
500 at AP4 and AP5 (Figs. 9B, 9C and 14). When C2b avulsed and became active (Fig. 14D), all
501 the up-dip channels segments formed a single conduit, with the result of the more up-dip
502 portions having acted as active conduits for increasing longer periods. Therefore, C2b, just
503 like C1b, shows significant variability in its dimension along its length and presents a stepped
504 decreasing trend downstream, with the AP4 being the major break (Figs. 11 and 14D). As for
505 the avulsion of C2c (Fig. 14E), it represent another example of aborted/incomplete avulsion

(Table 3); however, the difference with the C1c scenario is that the stop in sediment supply may have corresponded to the shut-off of the whole system, because C2c is the latest channel of the ACS. Such back-stepping and fore-stepping avulsion pattern documented in the ACS has analogues in the Amazon Fan (Pirmez and Flood, 1995; Pirmez et al., 1997) and the Northern Zaire Fan (Droz et al., 2003), and contrasts sharply with the distribution of avulsion points in Indus Fan (Kenyon et al., 1995) and Bengal Fan (Curray et al., 2003) where most avulsions have focused in a relatively restricted area forming a radial pattern.

6. Conclusions

(1) In the interval of interest, a MTC, six submarine channels and some lobe deposits developed in sequence. The MTC most likely originated from the failure of upslope regions and is mainly composed of remobilized material, interrupted by remnant blocks of the older stratigraphy.

(2) Channels of the ACS developed directly on the MTC and were confined by the remnant blocks and by the MTC lateral scarps. The areal extension of the MTC as well as the character of the debrites controlled the pathways of the submarine channels. Where MTC-related confinement was weak or decreased abruptly, the channels tended to develop higher sinuosity, increasing their instability and in turn resulting in the occurrence of avulsions.

(3) Three types of channel avulsions have been observed in the present study. Type 1 is characterised by parent and avulsion channel having similar size and maturity; Type 2 is characterised by a large, high-maturity parent channel and a small, low maturity avulsion channel; Type 3 emphasizes the larger scale and higher maturity of the avulsion channel compared to the parent channel. The five documented avulsion events of the ACS are classified accordingly.

(4) The temporal-spatial evolution of the ACS was divided into two phases; Phase I is characterised by the location of successive avulsion points shifting toward the shelf, whereas Phase II shows the opposite pattern.

(5) In the southern and distal part of the study area, mud diapirs created topography that captured turbidity flows which originated from two different avulsion points at different times, creating a channel confluence.

Acknowledgements

This study was supported by the National Natural Science Foundation of China (nos. 41872142, 41602145, 41602117), Science Research Starting Project of SWPU (no. 2014QHZ008), and Young Scholars Development Fund of SWPU (no. 201131010069). We are grateful to the China National Offshore Oil Company for allowing us to publish the seismic data. Also we thank two reviewers for the insigh reviews that greatly improve this paper.

References

Abreu, V., Sullivan, M., Pirmez, C., Mohrig, D., 2003. Lateral accretion packages (LAPs): an important reservoir element in deep water sinuous channels. Mar. Pet. Geol. 20, 631–648.

Adeogba, A.A., Mchargue, T.R., Graham, S.A., 2005. Transient fan architecture and depositional controls from near-surface 3-D data, Niger Delta continental slope. AAPG Bull. 89, 627–643.

Alfaro, E., Holz, M., 2014. Seismic geomorphological analysis of deepwater gravitydriven deposits on a slope system of the southern Colombian Caribbean margin. Mar. Pet. Geol. 57, 294-311.

555 Alves, M.T., 2015. Submarine slide blocks and associated soft-sediment deformation in deep-
556 wtar basins: A review. Mar. Pet. Geol. 67, 262-285.
557 Armitage, D.A., Romans, B.W., Covault, J.A., Graham, S.A., 2009. The influence of mass
558 transport deposit surface topography on the evolution of turbidite architecture: the Sierra
559 Contreras, Tres Pasos Formation (Cretaceous), southern Chile. J. Sediment. Res. 79,
560 287–301.
561 Armitage, D.A., McHargue, T., Fildani, A., Graham, S.A., 2012. Postavulsion channel
562 evolution: Niger Delta continental slope. AAPG Bull. 96, 823–843.
563 Ashabranner, L. B., E. K. Tripsanas, and R. C. Shipp. "Multi-direction flow in a mass-
564 transport deposit, Santos Basin, offshore Brazil." Submarine mass movements and their
565 consequences. Springer, Dordrecht, 2010. 247-255.
566 Bathurst, J.C., 1997. Environmental river flow hydraulics. In: Thorne, C.R., Hey, R.D.,
567 Newson, M.D. (Eds.), Applied Fluvial Geomorphology for River Engineering and
568 Management. John Wiley and Sons Ltd, pp. 69-93.
569 Best, J.L., Roy, A.G., 1991. Mixing-layer distortion at the confluence of channels of different
570 depth. Nature 350, 411-413.
571 Brami, T.R., Pirmez, C., Archie, C., Holman, K., 2000. Late Pleistocene deep-water
572 stratigraphy and depositional processes, offshore Trinidad and Tobago. In: Weimer, P.,
573 Slatt, R.M., Coleman, J., Rosen, N.C., Nelson, H., Bouma, A.H., Styzen, M.J.,
574 Lawrence, D.T. (Eds.), Deep-water Reservoirs of the World, Gulf Coast Section SEPM
575 20th Annual Research Conference, Port of Span, pp. 104–115.
576 Bull, S., Cartwright, J., Huuse, M., 2009. A review of kinematic indicators from
577 masstransport complexes using 3D seismic data. Mar. Pet. Geol. 26, 1132–1151.

578 Catterall, V., Redfern, J., Gawthorpe, R., Hansen, D., Thomas, M., 2010. Architectural style
579 and quantification of a submarine channel-levee system located in a structurally
580 complex area: offshore Nile Delta. J. Sediment. Res. 80, 991–1017.
581 Clark, I.R., Cartwright, J.A., 2009. Interactions between submarine channel systems and
582 deformation in deepwater fold belts: examples from the Levant Basin, Eastern
583 Mediterranean sea. Mar. Pet. Geol. 26, 1465 – 1482.
584 Cohen, H. A., Mcclay, K., 1996. Sedimentation and shale tectonics of the northwestern Niger
585 delta front. Mar. Pet. Geol. 13, 313–328.
586 Corella, J.P., Loizeau, J.L., Kremer, K., Hilbe, M., Gerard, J., Dantec, N., Stark, N.,
587 Gonzalez-Quijano, M., Giradclos, S., 2016. The role of mass-transport deposits and
588 turbidites in shaping modern lacustrine deepwater channels. Mar. Pet. Geol. 77, 515–525.
589 Curray, J.R., Moore, D.G., 1971. Growth of the Bengal deep-sea fan and denudation of the
590 Himalayas. Geol. Soc. Am. Bull. 82, 563 – 572.
591 Curray, J.R., Emmel, F.J., Moore, D.G., 2003. The Bengal Fan: morphology, geometry,
592 stratigraphy, history and processes. Mar. Pet. Geol. 19, 1191–1223.
593 Damuth, J.E., Kolla, V., Flood, R.D., Kowsmann, R.O., Monteiro, M.C., Gorini, M.A., Palma,
594 J.J.C., Belderson, R.H., 1983a. Distributary channel meandering and bifurcation patterns
595 on the Amazon deep-sea fan as revealed by long-range side-scan sonar (GLORIA).
596 Geology 11, 94–98.
597 Damuth, J.E., Kowsmann, R.O., Flood, R.D., Belderson, R.H., Gorini, M.A., 1983b. Age
598 relationships of distributary channels on Amazon deep-sea fan: implications for fan
599 growth pattern. Geology 11, 470–473.
600 Damuth, J.E., 1994. Neogene gravity tectonics and depositional processes on the deep Niger
601 Delta continental margin. Mar. Pet. Geol. 11, 320–346.

Deptuck, M.E., Steffens, G.S., Barton, M., Pirmez, C., 2003. Architecture and evolution of upper fan channel-belts on the Niger Delta slope and in the Arabian Sea. Mar. Pet. Geol. 20, 649-676.

Deptuck, M.E., Sylvester, Z., Pirmez, C., O'Byrne, C., 2007. Migration–aggradation history and 3-D seismic geomorphology of submarine channels in the Pleistocene Beninmajor Canyon, western Niger Delta slope. Mar. Pet. Geol. 24, 406-433.

Doust, H., Omatsola, E., 1989. Niger delta. In: Edwards, J.D., Santogrossi, P.A. (Eds.), Divergent/passive Margin Basins. American Association of Petroleum Geologists, Tulsa, pp. 201-238.

Droz, L., Marsset, T., Ondréas, H., Lopez, M., Savoye, B., Spy-Anderson, F.L., 2003. Architecture of an active mud-rich turbidite system: the Zaire Fan (Congo–Angola margin southeast Atlantic): results from ZaïAngo 1 and 2 cruises. AAPG Bull. 87, 1145–1168.

Dugan, B., Stigall, J., 2010. Origin of overpressure and slope failure in the Ursa Region, northern Gulf of Mexico. In: Mosher, D.C., Shipp, R.C., Moscardelli, L., Chaytor, J.D., Baxter, C.D.P., Lee, H.J., Urgeles, R. (Eds.), Submarine Mass Movements and Their Consequences. Springer, Netherlands, pp. 167-178.

Eggenhuisen, J.T., Mccaffrey, W.D., Haughton, P.D.W., Butler, R.W.H., Moore, I., Jarvie, A., Hakes, W.G., 2010. Reconstructing large-scale remobilisation of deepwater deposits and its impact on sand-body architecture from cored wells: the Lower Cretaceous Britannia Sandstone Formation, UK North Sea. Mar. Pet. Geol. 27, 1595–1615.

Fildani, A., Normark, W.R., 2004. Late Quaternary evolution of channel and lobe complexes of Monterey Fan. Mar. Geol. 206, 199 – 223.

625 Fildani, A., Normark, W.R., Kostic, S., Parker, G., 2006. Channel formation by flow
626 stripping: large-scale scour features along the Monterey East Channel and their relation
627 to sediment waves. Sedimentology 53, 1265 – 1287.
628 Fildani, A., Hubbard, S.M., Covault, J.A., Maier, K.L., Romans, B.W., Traer, M., Rowland,
629 J.C., 2013. Erosion at inception of deep-sea channels. Mar. Pet. Geol. 41, 48-61.
630 Flood, R.D., Manley, P.L., Kowsmann, R.O., Appi, C.J., Pirmez, C., 1991. Seismic facies
631 and late quaternary growth of Amazon submarine fan. In: Weimer, P., Link, M.H. (Eds.),
632 Seismic Facies and Sedimentary Process of Submarine Fans and Turbidite Systems.
633 Springer, New York, pp. 415-433.
634 Gamboa, D., Alves, T., Cartwright, J., Terrinha, P., 2010. Mass-transport deposits
635 distribution on a 'passive' continental margin: the Espírito Santo Basin (SE Brazil)
636 during the Palaeogene. Mar. Pet. Geol. 27 (7), 1311-1324.
637 Gamboa, D., Alves, T., Cartwright, J., 2012. A submarine channel confluence classification
638 for topographically confined slopes. Mar. Pet. Geol. 35, 176-189.
639 Gamboa, D., Alves, T., 2016. Bi-modal deformation styles in confined mass-transport
640 deposits: Examples from a salt minibasin in SE Brazil. Mar. Geol. 379, 176-193.
641 Gee, M.J.R., Gawthorpe, R.L., Bakke, K., Friedmann, S.J., 2007. Seismic geomorphology
642 and evolution of submarine channels from the Angolan continental margin. J. Sediment.
643 Res. 77, 433-446.
644 Gong, C.L., Wang, Y.M., Hodgson, D.M., Zhu, W.L., Li, W.G., Xu, Q., Li, D., 2014. Origin
645 and anatomy of two different types of mass-transport complexes: A 3D seismic case
646 study from the northern South China Sea margin. Mar. Pet. Geol. 54, 198-215.
647 Grozic, J.L.H., 2010. Interplay between gas hydrates and submarine slope failure. In: Mosher,
648 D.C., Shipp, R.C., Moscardelli, L., Chaytor, J.D., Baxter, C.D.P., Lee, H.J., Urgeles, R.

(Eds.), Submarine Mass Movements and Their Consequences. Springer, Netherlands, pp. 11-30.

Hansen, L., L'Heureux, J.S., Sauvin, G., Polom, G. Lecomte, I., Vaveste, M., Longva, O., Krawczyk, C., 2013. The effect of mass-wasting on the stratigraphic architecture of a fjord-valley fill: correlation of onshore, shear wave seismics and marine seismic data at Trondheim, Norway. Sediment. Geol. 289, 1–18.

Jackson, C.A.L., Johnson, H.D., 2009. Sustained turbidity currents and their interaction with debrite-related topography: Labuan Island, offshore NW Borneo, Malaysia. Sediment. Geol. 219, 77–96.

Joane, C., Collot, J.Y., Lamarche, G., Migeon, S., 2010. Continental slope reconstruction after a giant mass failure, the example of the Matakaoa margin, New Zealand. Mar. Geol. 268, 67–84.

Jolly, B.A., Lonergan, L., Whittaker, A.C., 2016. Growth history of fault-related folds and interaction with seabed channels in the toe-thrust region of the deep-water niger delta. Mar. Pet. Geol. 70, 58-76.

Kenyon, N.H., Amir, A., Cramp, A., 1995. Geometry of the younger sediment bodies of the Indus Fan. In: Pickering, K.T., Hiscott, R.N., Kenyon, N.H., Lucchi, F.R., Smith, R.D.A. (Eds.), Atlas of Deep Water Environments. Springer, Netherlands, pp. 89–93.

Kneller, B., Dykstra, M., Fairweather, L., Milana, J.P., 2016. Mass-transport and slope accommodation: implications for turbidite sandstone reservoirs. AAPG Bull. 100, 213–235.

Kolla, V., Coumes, F., 1987. Morphology, internal structure, seismic stratigraphy, and sedimentation of Indus Fan. AAPG Bull. 71, 650–677.

Kolla, V., 2007. A review of sinuous channel avulsion patterns in some major deep-sea fans and factors controlling them. Mar. Pet. Geol. 24, 450–469.

Kostic, S., 2011. Modeling of submarine cyclic steps: controls on their formation, migration, and architecture. Geosphere 7, 294 – 304.

Liu, L., Zhang, T., Zhao, X., Wu, S., Hu, J., Wang, X. Zhang, Y., 2013. Sedimntary architecture models of deep-water turbidite channel systems in the Niger Delta continental slope, West Africa. Petrol. Sci. 10, 139-148.

Maier, K.L., Fildani, A., Paull, C.K., McHargue, T.R., Graham, S.A., Caress, D.W., Talling, P., 2013. Deep-sea channel evolution and stratigraphic architecture from inception to abandonment from high-resolution Autonomous Underwater Vehicle surveys offshore central California. Sedimentology 60, 935–960.

Manley, P.L., Flood, R.D., 1988. Cyclic deposition within Amazon deep-sea fan. AAPG Bull. 72, 912–925.

Masalimova, L., Lowe, D.R., Mchargue, T., Derksen, R., 2015. Interplay between an axial channel belt, slope gullies and overbank deposition in the Puchkirchen Formation in the Molasse Basin, Austria. Sedimentology 62, 1717–1748.

Maslin, M., Owen, M., Day, S., Long, D., 2004. Linking continental-slope failures and climate change: testing the clathrate gun hypothesis. Geology 32 (1), 53-56.

Masson, D.G., Wynn, R.B., Talling, P.J., 2010. Large landslides on passive continental margins: processes, hypotheses and outstanding questions. In: Mosher, D.C., Shipp, R.C., Moscardelli, L., Chaytor, J.D., Baxter, C.D.P., Lee, H.J., Urgeles, R. (Eds.), Submarine Mass Movements and Their Consequences. Springer, Netherlands, pp. 153-166.

Mitchell, N.C., 2004. Form of submarine erosion from confluences in Atlantic USA continental slope Canyons. Am. J. Sci. 304, 590-611.

Morley, C.K., Guerin, G., 1996. Comparison of gravitydriven deformation styles and behavior associated with mobile shales and salt: Tectonics 15, 1154–1170.

699 Moscardelli, L., Wood, L., Mann, P., 2006. Mass-transport complexes and associated
700 processes in the offshore area of Trinidad and Venezuela. AAPG Bull. 90, 1059–1088.
701 Mulder, T., Ducassou, E., Gillet, H., Hanquiez, V., Tournadour, E., Combes, J., Eberli, G.P.,
702 Kindler, P., Gonthier, E., Conesa, G., 2012. Canyon morphology on a modern carbonate
703 slope of the Bahamas: evidence of regional tectonic tilting. Geology 40, 771–774.
704 Nakajima, T., Kneller, B.C., 2013. Quantitative analysis of the geometry of submarine
705 external levées. Sedimentology 60, 877–910.
706 Normark, W.R., 1978. Fan vallys, channels, and depositional lobes on modern submarine
707 fans: characters for recognition of sandy turbidite environments. AAPG Bull. 61, 912-
708 931.
709 Olafiranye, K., Jackson, A.L., Hodgson, D.M., 2013. The role of tectonics and mass-transport
710 complex emplacement on upper slope stratigraphic evolution: a 3D seismic case study
711 from offshore Angola. Mar. Pet. Geol. 44, 196–216.
712 Ortiz-Karpf, A., Hodgson, D.M., McCaffrey, W.D., 2015. The role of mass-transport
713 complexes in controlling channel avulsion and the subsequent sediment dispersal
714 patterns on an active margin: the Magdalena Fan, offshore Colombia. Mar. Pet. Geol. 64,
715 58–75.
716 Ortiz-Karpf, Hodgson, D.M., Jackson, C.A., McCaffrey, W.D., 2017. Influence of seabed
717 morphology and substrate composition on mass-transport flow process and pathways:
718 Insights from the Magdalena Fan, offshore Colombia. J. Sediment. Res. 87, 189-209.
719 Piper, D.J.W., Normark, W.R., 1983. Turbidite depositional patterns and flow characteristics,
720 Navy Submarine Fan, California Borderland. Sedimentology 30, 681–694.
721 Pirmez, C., Flood, D.R., 1995. Morphology and structure of Amazon channel. In: In: Flood,
722 R.D., Piper, D.J.W., Klaus, A., Peterson, L.C. (Eds.), Proceedings of the Ocean Drilling
723 Program, Initial Reports, vol. 155. pp. 23–45.

724 Pirmez, C., Hiscott, R.N., Kronen, J.D., 1997. Sandy turbidite successions at the base of
725 channel-levee systems of the Amazon Fan revealed by FMS logs and cores: unraveling
726 the facies architecture of large submarine fans. In: In: Flood, R.D., Piper, D.J.W., Klaus,
727 A., Peterson, L.C. (Eds.), Proceedings of the Ocean Drilling Program, Scientific Results,
728 vol. 155. pp. 7–33.
729 Posamentier, H.W., Kolla, V., 2003. Seismic geomorphology and stratigraphy of depositional
730 elements in deep-water settings. J. Sediment. Res. 73, 367–388.
731 Posamentier, H.W., 2004. Stratigraphy and geomorphology of deep-water mass-transport
732 complexes based on 3D seismic data. Proceedings of the Annual Offshore Technology
733 Conference.
734 Posamentier, H.W., Davies, R.J., Cartwright, J.A., Wood, L., 2007. Seismic geomorphology-
735 an overview. In: In: Davies, R.J., Posamentier, H.W., Wood, L.J., Cartwright, J.A.
736 (Eds.), Seismic Geomorphology: Applications to Hydrocarbon Exploration and
737 Production, vol. 277. Geological Society, London, Special Publications, pp. 1–14.
738 Prather, B.E., 2000. Calibration and visualization of depositional process models for above-
739 grade slopes: a case study from the Gulf of Mexico. Mar. Pet. Geol. 17, 619 – 638.
740 Qin, Y.P., Alves, T.M., Constantine, J., Gamboa, D., 2017. The role of mass wasting in the
741 progressive development of submarine channels (Espirito Santo Basin, SE Brazil). J.
742 Sediment. Res. 87, 500-516.
743 Saller, A., Dharmasamadhi, I.N.W., 2012. Controls on the development of valleys, canyons,
744 and unconfined cannel-levee complexes on the Pleistocene Slope of East Kalimantan,
745 Indonesia. Mar. Pet. Geol. 29, 15-34.
746 Short, K.C., Stäuble, A.J., 1967. Outline of geology of Niger delta. AAPG Bull. 51, 761–779.

Straight, L., Bernhardt, A., Boucher, A., 2013. DFTopoSim: modeling topographically-controlled deposition of subseismic scale sandstone packages within a mass transport dominated deep-water channel belt. Math. Geosci. 45, 277–296.

Vail, P.R., Mitchum, R.M.J., Thompson, S., 1977. Seismic stratigraphy and global changes of sea level, Part 3: relative changes of sea level from coastal onlap. In: Payton, C.E. (Ed.), Seismic Stratigraphy-application to Hydrocarbon Exploration. American Association of Petroleum Geologists, Oklahoma, pp. 63–82.

Wang, K.H., Cleveland, T.G., Fitzgerald, S., Ren, X., 1996. Hydrodynamic flow modeling at confluence of two streams. J. Eng. Mech. 122, 994.

Ward, I.P.N., Alves, M.T., Blenkinsop, G.T., 2018. Submarine sediment routing over a blocky mass-transport deposit in the Espirito Santo Basin, SE Brazil. Basin. Res. 30, 816-834.

Weimer, P., Slatt, R.M., 2007. Introduction to the Petroleum Geology of Deep-water Settings. In: AAPG Memoir, pp. 419-456.

Wiles, E., Green, A., Watkeys, M., Jokat, W., 2017. The Zambezi Channel： A new perspective on submarine channel evolution at low latitudes. Geomorphology 286, 121-132.

Zhao, X.M., Qi, K., Liu, L., Gong, C.L., McCaffrey, W.D., 2018a. Development of a partially-avulsed submarine channel on the Niger Delta continental slope: Architecture and controlling factors. Mar. Pet. Geol. 95, 30-49.

Zhao X.M., Qi, K., Liu, L., Xie, T., Li, M.H., Hu, G.Y., 2018b. Quantitative characterization and controlling factor analysis of the morphology of Bukuma-minor Channel on southern Niger Delta slope. Intepretation-J. Sub. 6, 57-69.

Zhang, J., Wu, S., Wang, X., Lin, Y., Fan, H., Jiang, L., Wan, Q., Yin, H., Lu, Y., 2015. Reservoir quality variations within a sinuous deep water channel system in the Niger Delta Basin, offshore west Africa. Mar. Pet. Geol. 63, 166–188.

Zucker, E., Gvirtzman, Z., Steinberg, J., Enzel, Y., 2017. Diversion and morphology of submarine channels in response to regional slopes and localized salt tectonics, Levant basin. Mar. Pet. Geol. 81, 98–111.

Table 1
Descriptions and interpretations of the seismic facies defined in this study.

	Seismic facies	Description	Interpretation
①	Variable-amplitude, discontinuous reflectors	Variable-amplitude, discontinuous reflectors are confined within a V-shaped or U-shaped surface. They are elongated and sinuous in map view, and are bounded on either side by facies 2.	Channel fills (Abreu et al., 2003; Posamentier and Kolla, 2003; Gee et al., 2007)
②	Low-amplitude, continuous reflectors in wedge-shaped packages	Low-amplitude, continuous reflectors in wedge-shaped packages that pinch out over a certain distance. The reflectors downlap or onlap older packages and are found on either side of facies 1. In map view, they are also elongated and trend parallel to facies 1.	External levee deposits (Deptuck et al., 2003; Nakajima and Kneller, 2013; Zhao et al., 2018)
③	Low-amplitude, discontinuous, chaotic reflectors	Chaotic, discontinuous reflectors; they dip in different directions and at different angles. They have erosional bases and irregular tops.	MTC remobilized deposits (Gong et al., 2014; Ortiz-Karpf et al., 2015). MTC debrites/matrixes (Bull et al., 2009; Gamboa et al., 2011)
④	Parallel, high-amplitude, continuous reflectors	Parallel, high amplitude reflectors; they constitute a continuous package that extends across most of the study area.	Lobe deposits (Weimer and Slatt, 2007; Saller and Dharmasamadhi, 2012;)
⑤	Variable-amplitude, continuous, irregular-shaped reflectors	Packages surrounded by facies 3 with irregular-shaped geometries; they are often north-south-trending blocks composed of parallel, variable-amplitude, continuous reflectors.	Erosional shadow remnants of MTC (sensu Moscardelli et al., 2006). Remnant ridges of MTC (sensu Ortiz-Karpf et al., 2015). Remnant blocks of MTC (Gamboa et al., 2011; Ward et al., 2018)

Table 2

Quantitative parameters of submarine channels discussed in the present study.

Channel	Width/AF (m)	Height/AF (m)	Cross-sectional area/AF (m^2)	Sinuosity	Levees
C1a	213-275/62	41-55/14	4750-9351/4601	1.12	No
C1b	137-540/403	30-85/55	2227-30114/27887	1.21	Yes in the upstream reach
C1c	123-180/57	24-44/20	1900-6234//4334	1.04	No
C2a	150-437/287	32-72/40	3117-14992/11875	1.09	No
C2b	391-637/246	58-108/50	13656-38890/25234	1.17	Yes
C2c	110-212/102	24-50/26	2565-8460/5895	1.08	No

AF = amplitude of fluctuation = maximum value-minimum value

Table 3
Characteristics of the five avulsion points (AP).

Avulsion point	Parent channel	Avulsion channel	Avulsion type
Ap1	C1a	C1b	Type 1
Ap2	C1b	C1c	Type 2
Ap3	C1b	C2a	Type 1
Ap4	C2a	C2b	Type 3
Ap5	C2b	C2c	Type 2

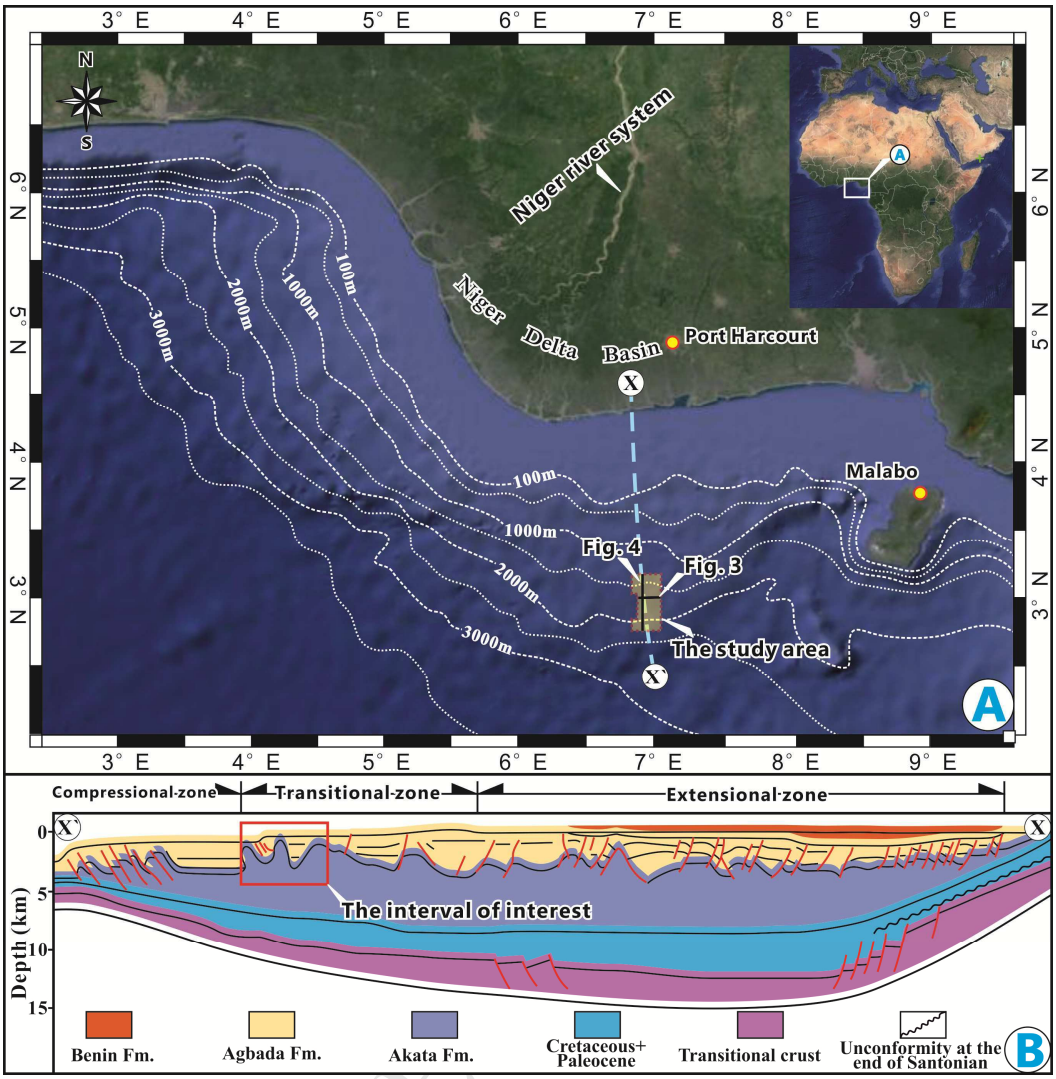

Fig. 1. (A) Location map of the study area; white dashed lines represent water depth contours (modified after Adeogba et al. 2005). The study area (yellow box) is located in a middle continental slope, with a water depth range of 1300-1700 m. (B) Cross section of the Niger Delta Basin showing three structural zones (extensional, transitional, and compression zones) from north to south (modified after Zhang et al., 2015). The study area lies in the most basinward part of the transitional zone,

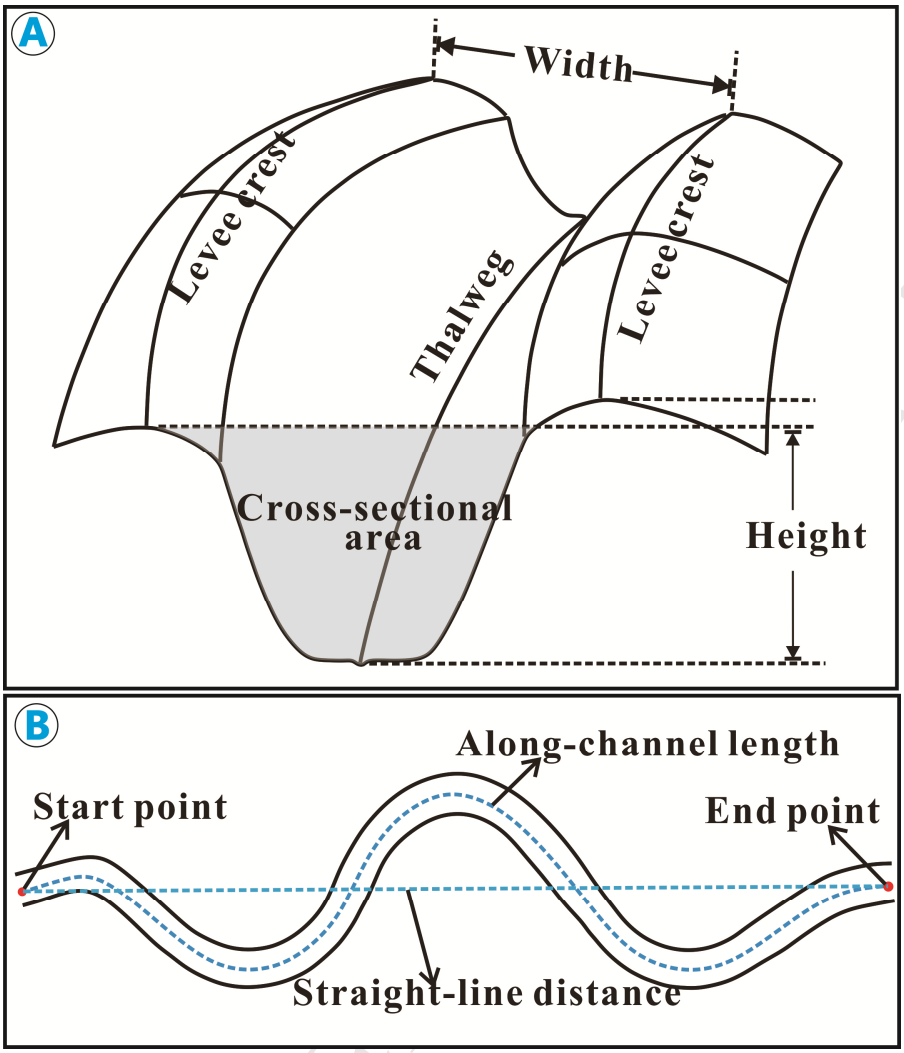

Fig. 2. Sketch diagram illustrating the geometrical parameters used to define (A) width, height, cross-sectional area (modified from Wiles et al., 2017) and (B) sinuosity. The width is the horizontal distance between levee crests (or the distance between two banks when there is no noticeable levee); the height is the vertical distance between the lower levee crest (or the lower bank of the erosional surface when there is no recognized levee) and the deepest point of the submarine channel. To concisely present the morphometrics of submarine channels, the above figure only shows the more complex scenario, i.e. leveed submarine channels. Note that when measuring these parameters, the seismic profile should be perpendicular to the flow direction. Only one sinuosity value was calculated for each channel, defined as the ratio of the along-channel length to the straight-line distance between its end points.

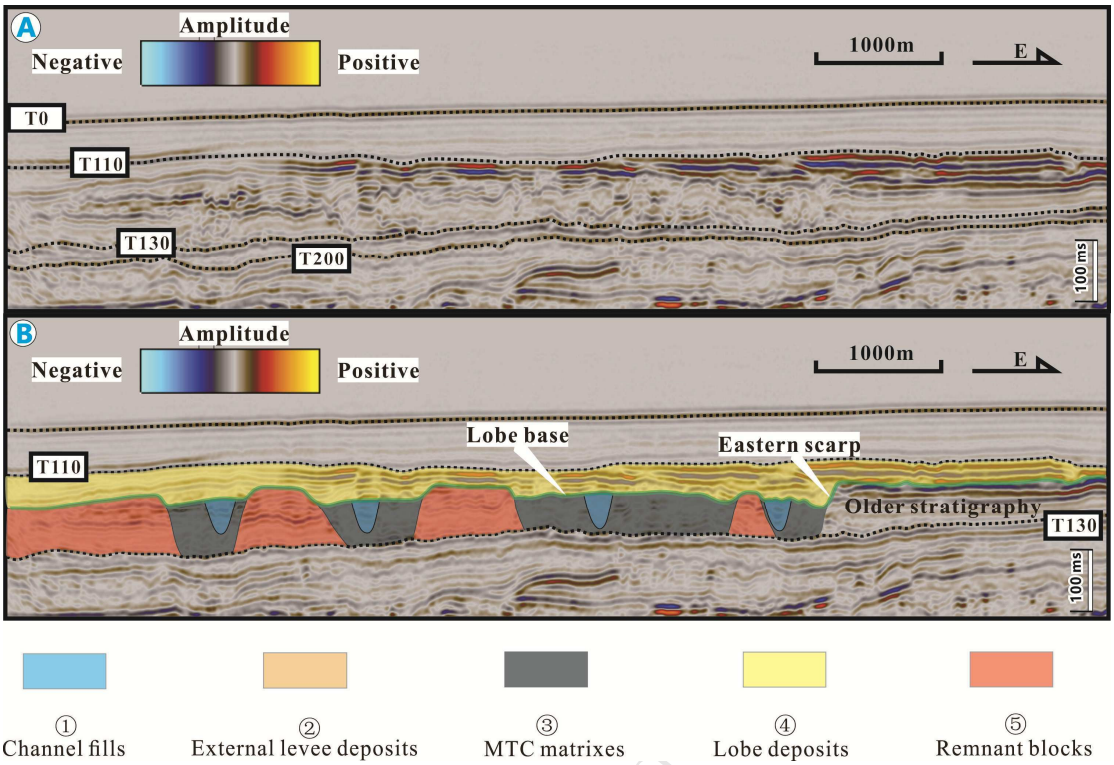

Fig. 3. (A) Uninterpreted and (B) interpreted strike-view seismic section (for line location see Fig. 5) showing the stratigraphic architecture of the study area and the seismic facies documented in the interval of interest. Four surfaces (T0, T110, T130, and T200) were tracked in the shallow subsurface of the study area; the study interval is bounded by T110 and T130.

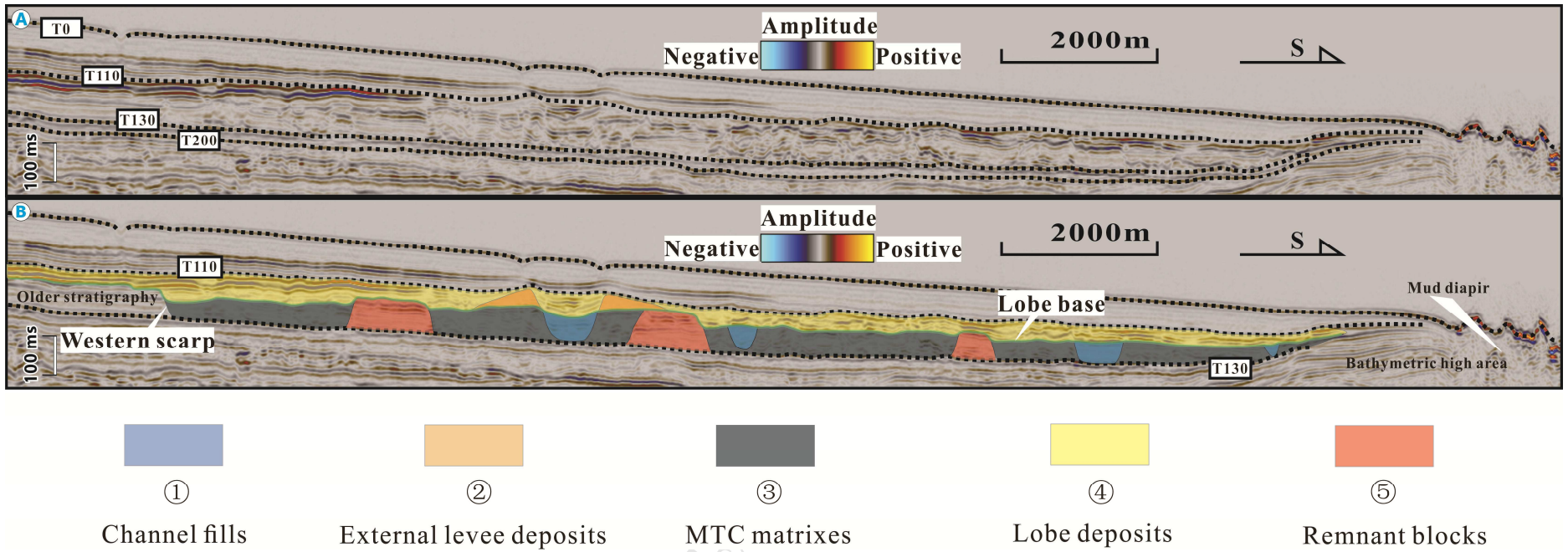

Fig. 4. (A) Uninterpreted and (B) interpreted dip-view seismic sections (for line location see Fig. 5) showing the stratigraphic architecture of the study area and the seismic facies documented in the interval of interest. Four seismic surfaces that are tracked in the strike-oriented profile (Fig. 3) are also shown in this section. Note that in the distal part of the study area there are well-developed mud diapirs and they are deduced to be antecedent or contemporary to the deposition of the studied interval because all considered intervals taper out toward them.

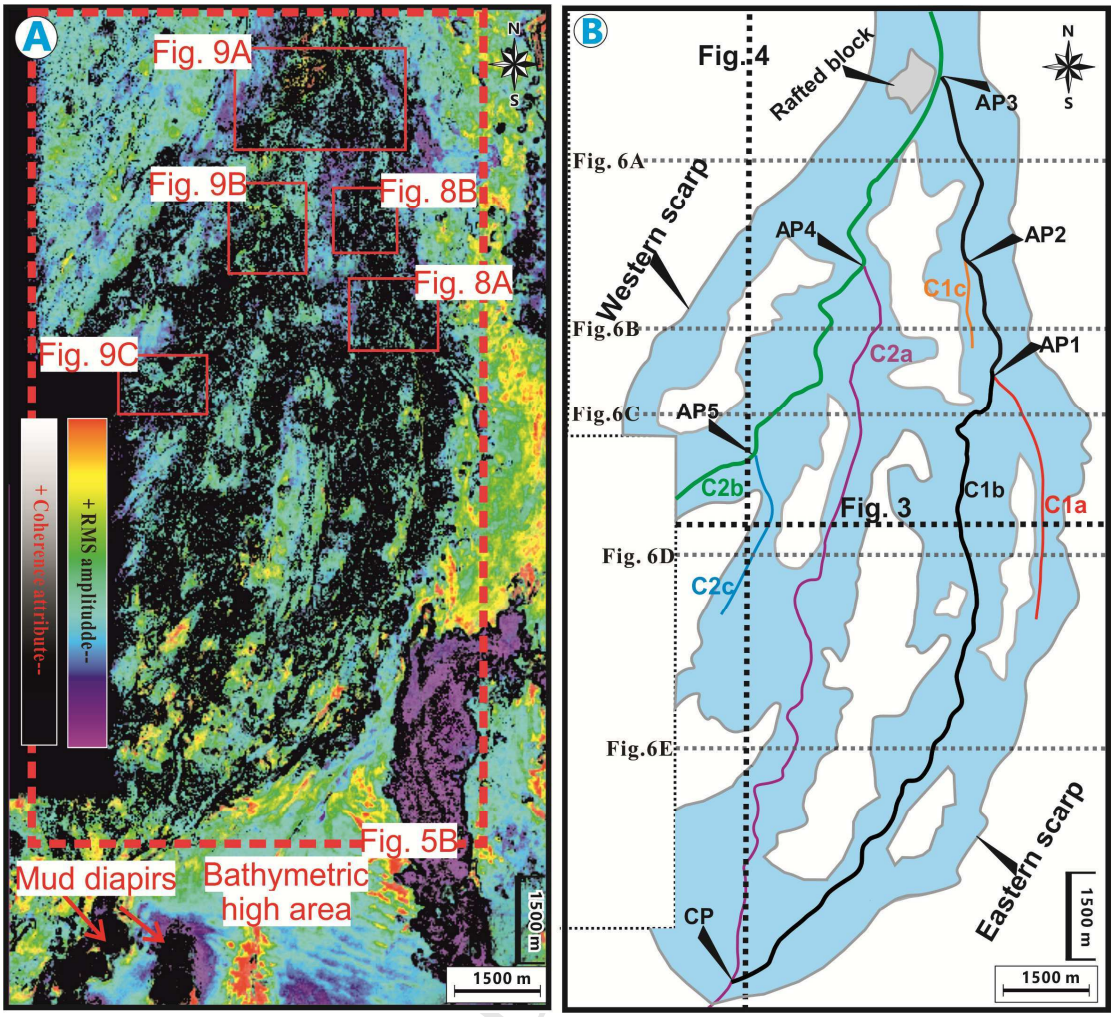

Fig. 5. (A) Combined display of the root mean square amplitude map and the coherence attribute map of the study area extracted from the interval of interest (T110-T130). (B) Interpretation of the study area, showing the extent of the MTC and the channel network of the 'Ablama Channel System' (ACS). Note that the white patches enclosed by the MTC matrixes are interpreted as remnant blocks and the grey patch recognized in northernmost part is a rafted block. The ACS consists of six channel segments, C1a through C2c delimited by five avulsion points, AP1 to AP5. The channels directly overlie the MTC and are confined by the remnant blocks or by the lateral scarps of the MTC. In the down-dip portion of the studied area, C1b and C2a join at a confluence point (CP) and the resulting channel continues outside of the study area. AP = avulsion point; CP = confluence point.

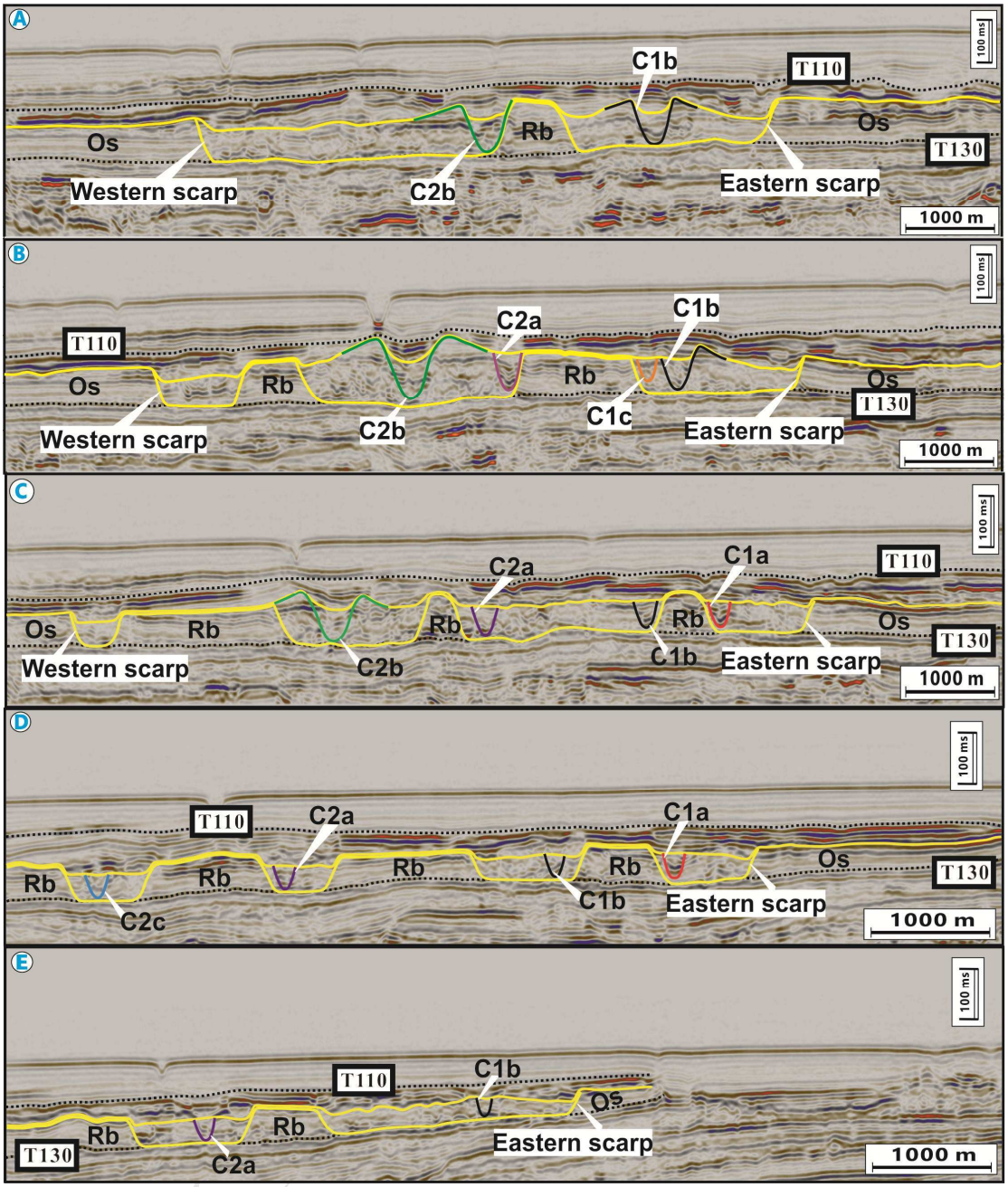

Fig. 6. A series of strike-view seismic profiles showing the down-slope changes of MTC and submarine channels (see Fig. 5B for lines location). The upper and lower yellow solid lines denote the basal surface of the lobe deposits and that of the MTC, respectively; note that these two surfaces coincide on remnant blocks. Overlain by lobe deposits, the submarine channels incised into MTC matrixes and are confined by remnant blocks or lateral scarps. Os = Older stratigraphy; Rb = Remnant blocks.

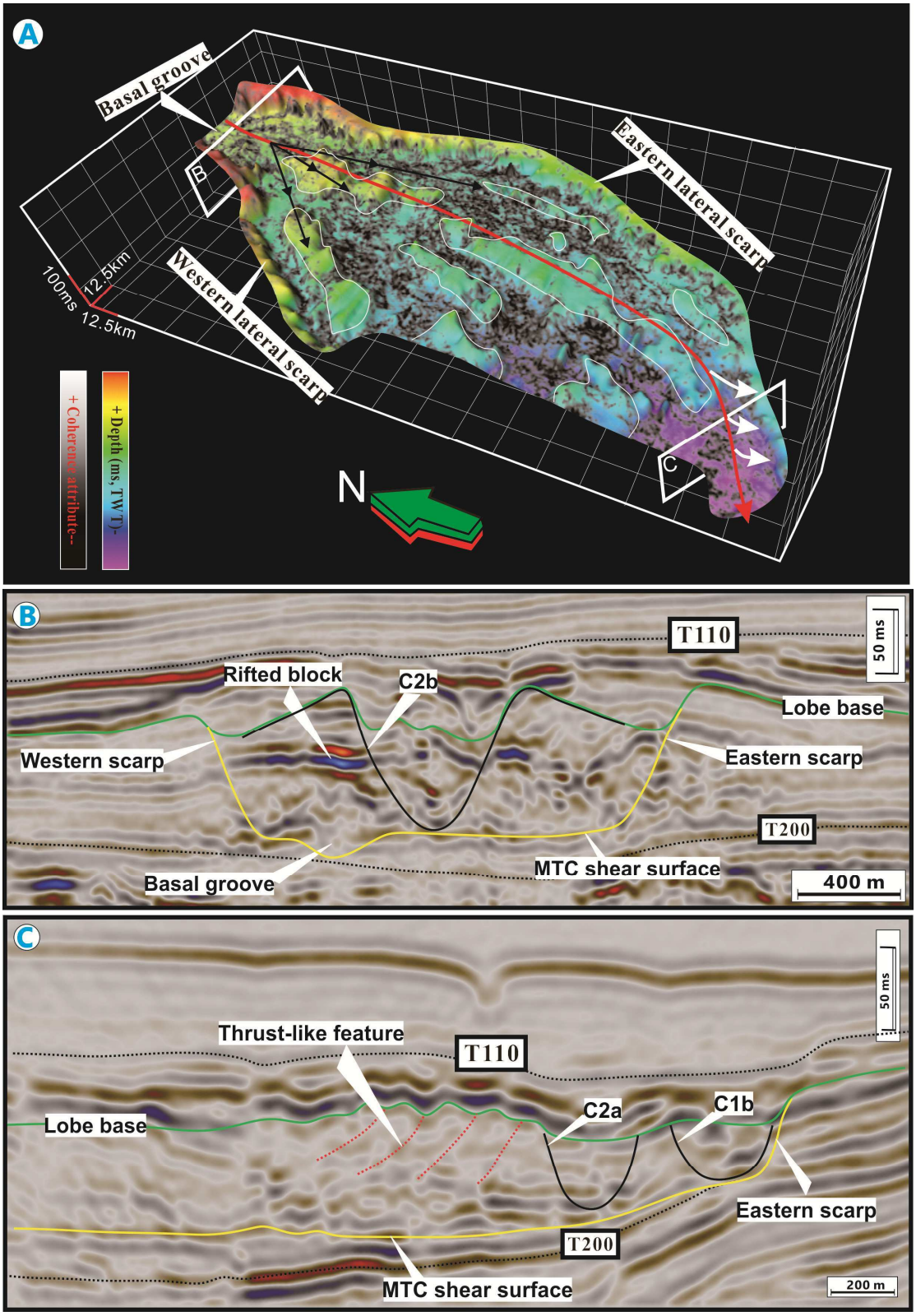

Fig. 7. (A) Coherence map extracted from the study interval (scale of greys), overlain on the MTC basal surface (coloured by depth). In the northernmost and more proximal part, the MTC seems to be confined by a U-shaped surface. However, a short distance downstream it appears to spread out in an unconfined domain. The main axes of the three remnant blocks (black arrows) can be traced back to a point that might represent where confinement was reduced or lost. The red arrow refers

to the main axis of elongation of the MTC, which tends to be deflected toward the southwest due to the presence of mud diapirs. White arrows indicate direction of thrusting against the mud diapirs. (B) Seismic profile across the proximal confined area of the MTC. Only in this area, a basal groove and the corresponding rifted block can be recognized. (C) Seismic profile in the diversion area of MTC showing thrust-like feature against the bathymetric high imposed by mud diapirs.

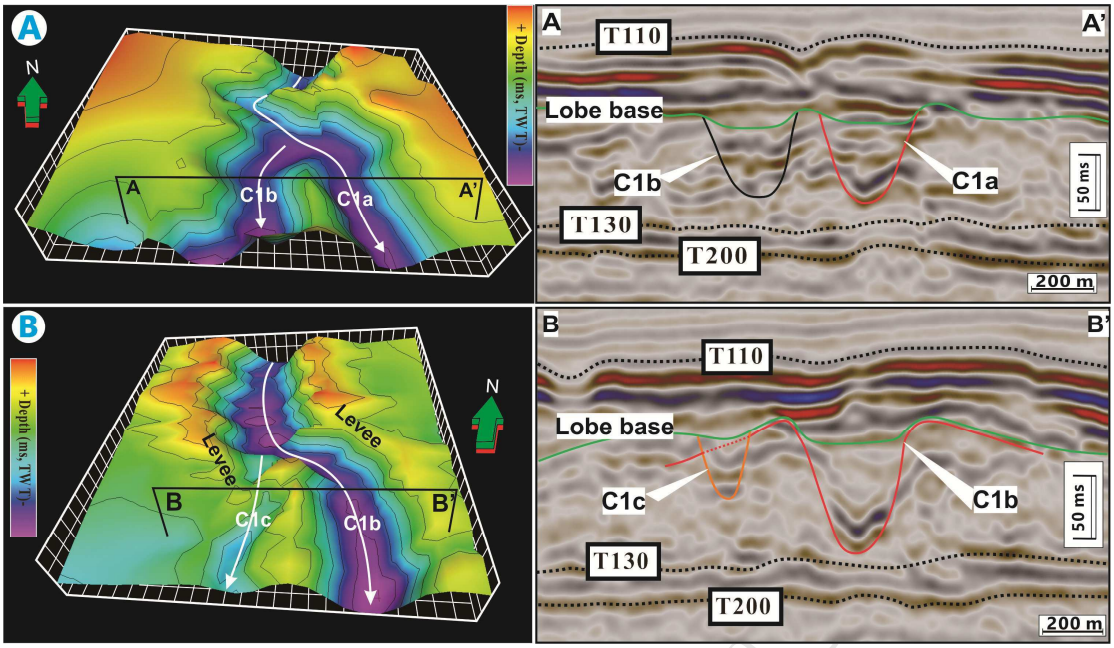

Fig. 8. Two-way traveltime (TWT) structural maps of the channel bounding surfaces at AP1 (A) and AP2 (B) and associated seismic sections. (A) Near AP1, C1b originated from the outside of a sharp bend of C1a. (B) Near AP2, C1c originated from a sharp bend of C1b and directly developed on its right levee. Hence, we can get the conclusion that C1a, C1b, C1c and associated AP1 and AP2 came into existence in chronological order.

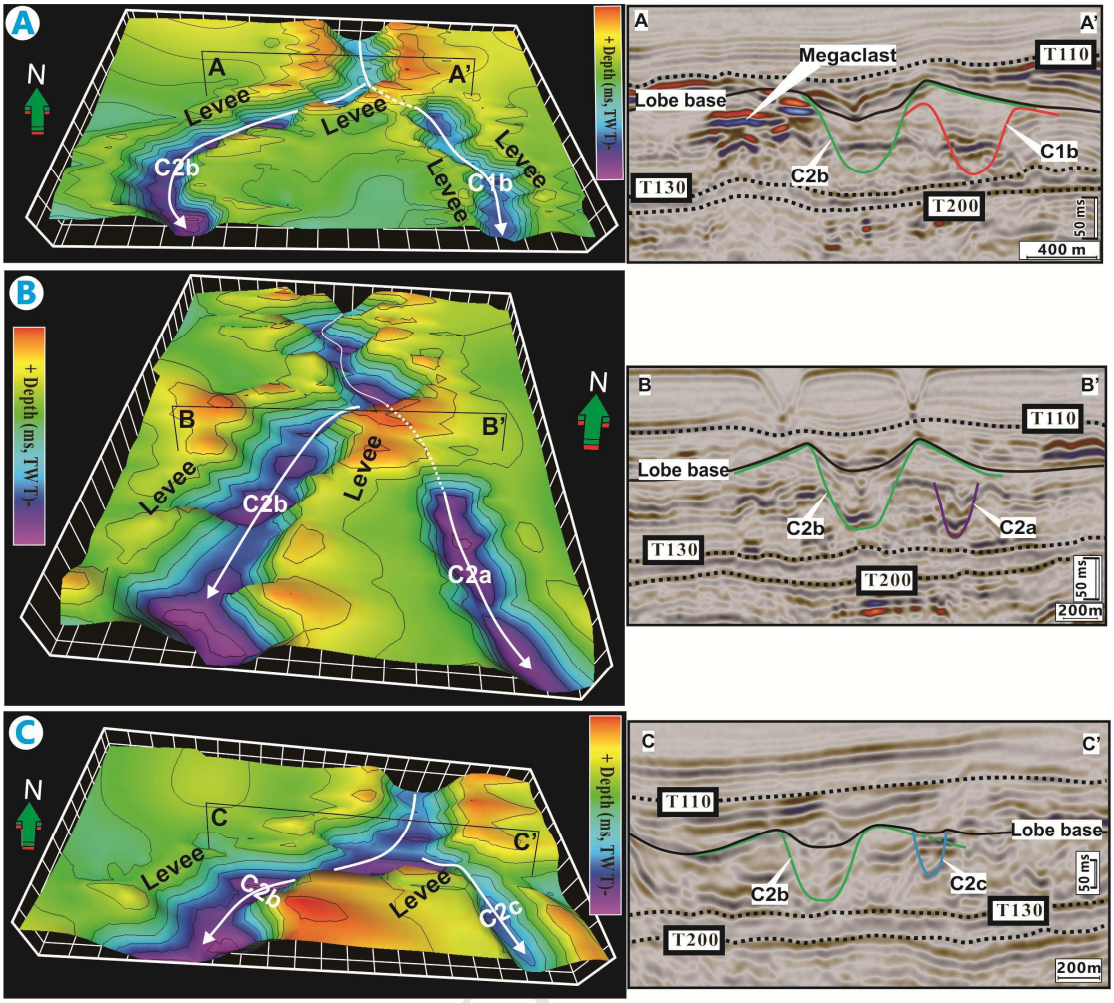

Fig. 9. Two-way traveltime (TWT) structural maps of the channel bounding surfaces at AP3 (A), AP4 (B) and AP5 (C) and associated seismic sections. (A) At AP3, C2b had partially eroded the right levee of C1b and its left levee directly overlie C1b channel head. (B) At AP4, the left levee of C2b had also overlain C2a channel head. (C) At AP5, C2c originated from the sharp bend of C2b and developed on its left levee, similar to the configuration at AP2 (Fig. 8B). Therefore, it could be deduced out that after the formation of C1a-C1c, C2a, C2b, C2c and associated AP3, AP4 and AP5 successively showed up.

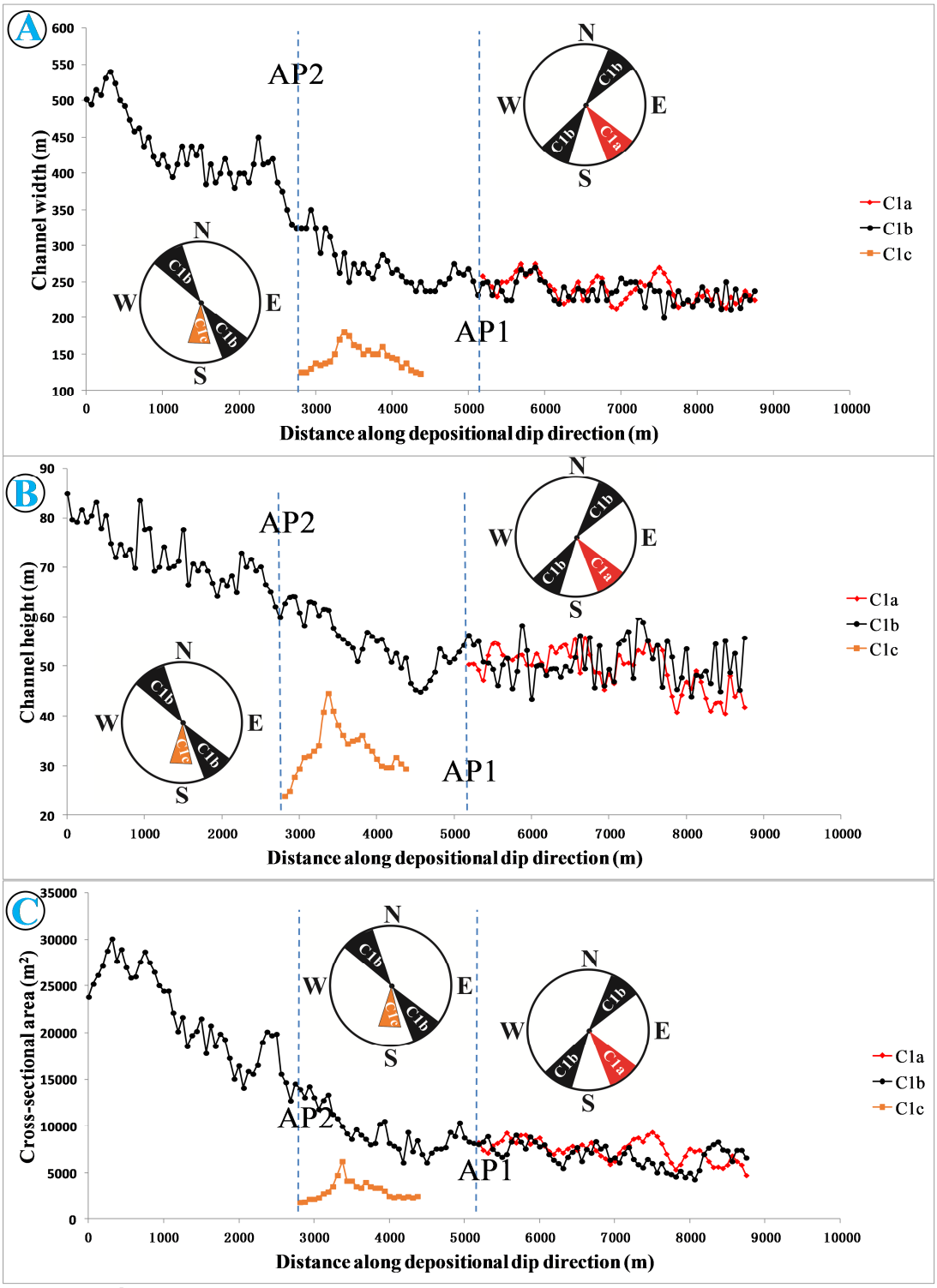

Fig. 10. Quantitative analyses of C1a, C1c, and part of C1b, showing their down-channel changes in widths (A), heights (B) and cross-sectional areas (C). The x-axis refers to the distance along the depositional dip direction (the North-South direction) of the ACS, with the origin representing the proximal end of C1b (AP3 in Figure 5). The position of avulsion points AP1 and AP2 is shown by vertical dashed lines. Compass circles for each avulsion point include triangles that show the direction and an indication of relative size of the parent and of the avulsed channel around the avulsion point. Note that C1a and C1b are comparable in size around AP1, however, C1c is rather

smaller than C1b near AP2, though it presents significant size variations along the depositional dip direction.

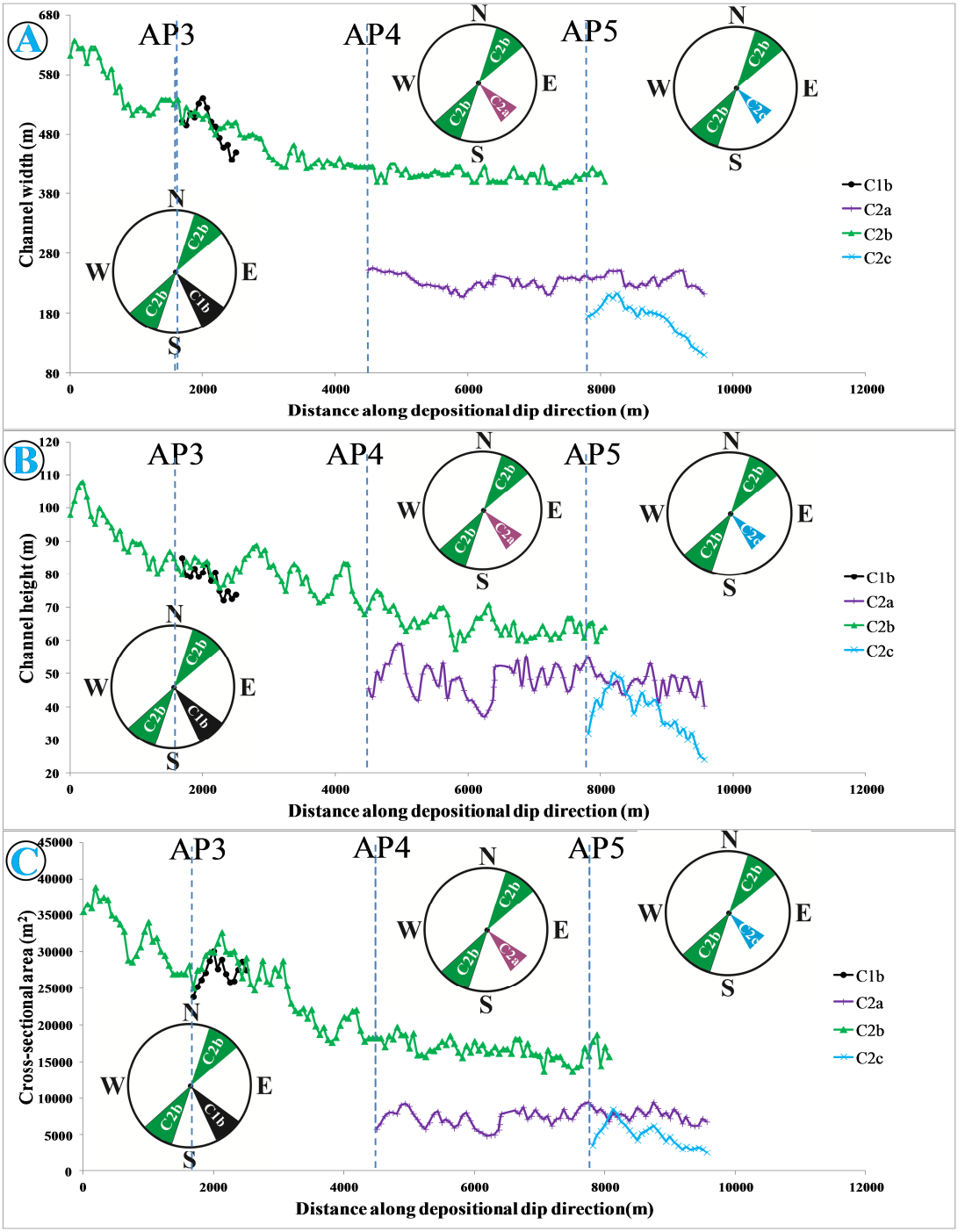

Fig. 11. Quantitative analyses of the C2b, C2c and part of C2a, showing their down-channel changes in widths (A), heights (B) and cross-sectional areas (C). The origin of the x-axis refers to the northernmost limit of the study area (note this is different in Fig. 10). Data from the headwall part of C1b are also shown (full data in Fig. 10), to help compare the parent channel and the avulsion channel around AP3. Note that C2b and C1b are comparable in scale around AP3, however, the scales of C2a as well as C2c are rather smaller than that of C2b around AP4 and AP5. For the meaning of the compass circles, see Figure 10.

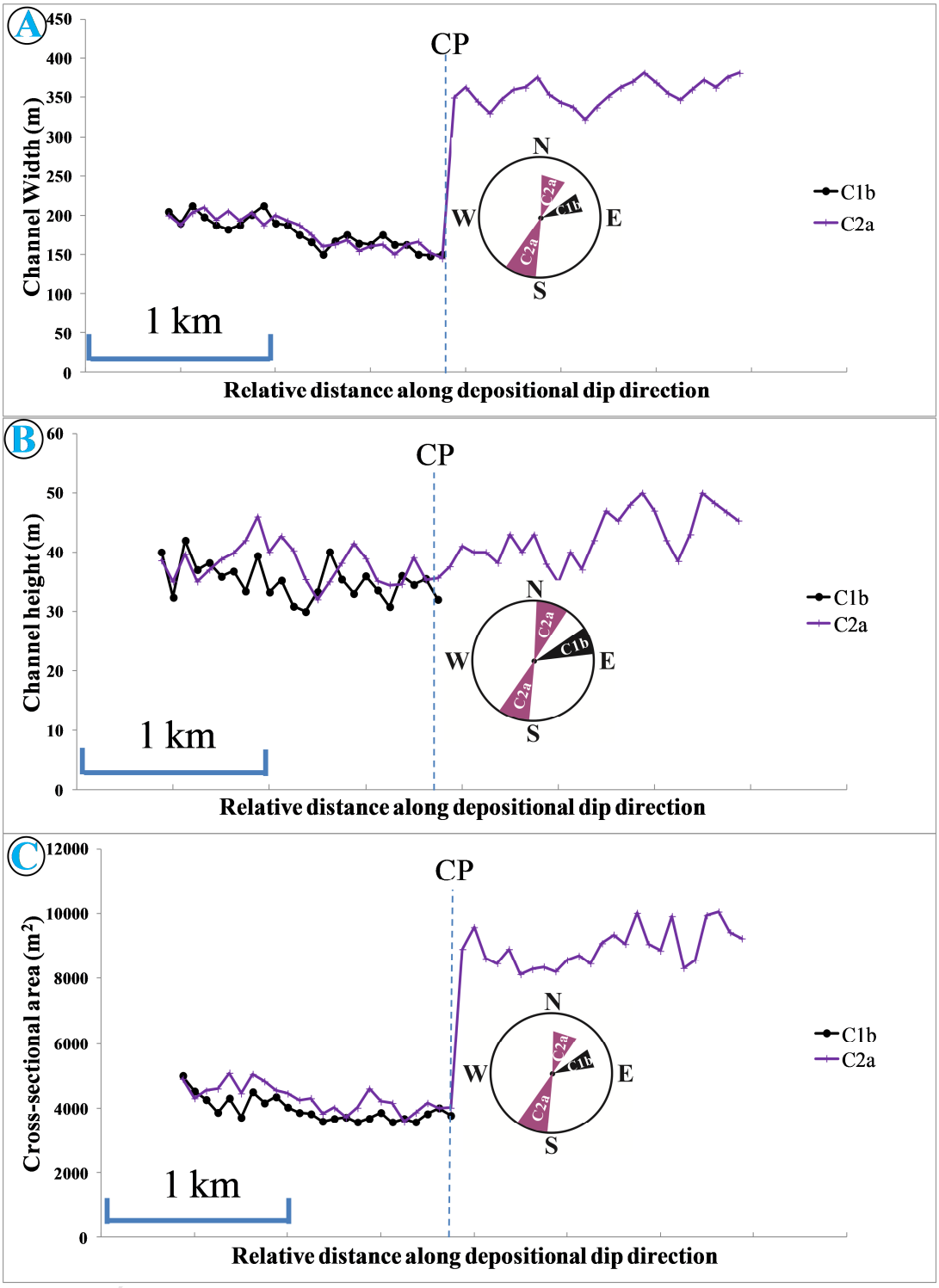

Fig. 12. Downstream changes in widths (A), heights (B) and cross-sectional areas (C) around the confluence point (CP) for C1b and C2a. The origin of the x-axis is about 2 km north of the confluence point. Note how the width and cross-sectional area of C2a increase abruptly down-dip of the confluence point, while the channel height does not show any significant change. For the meaning of the compass circles, see Figure 10.

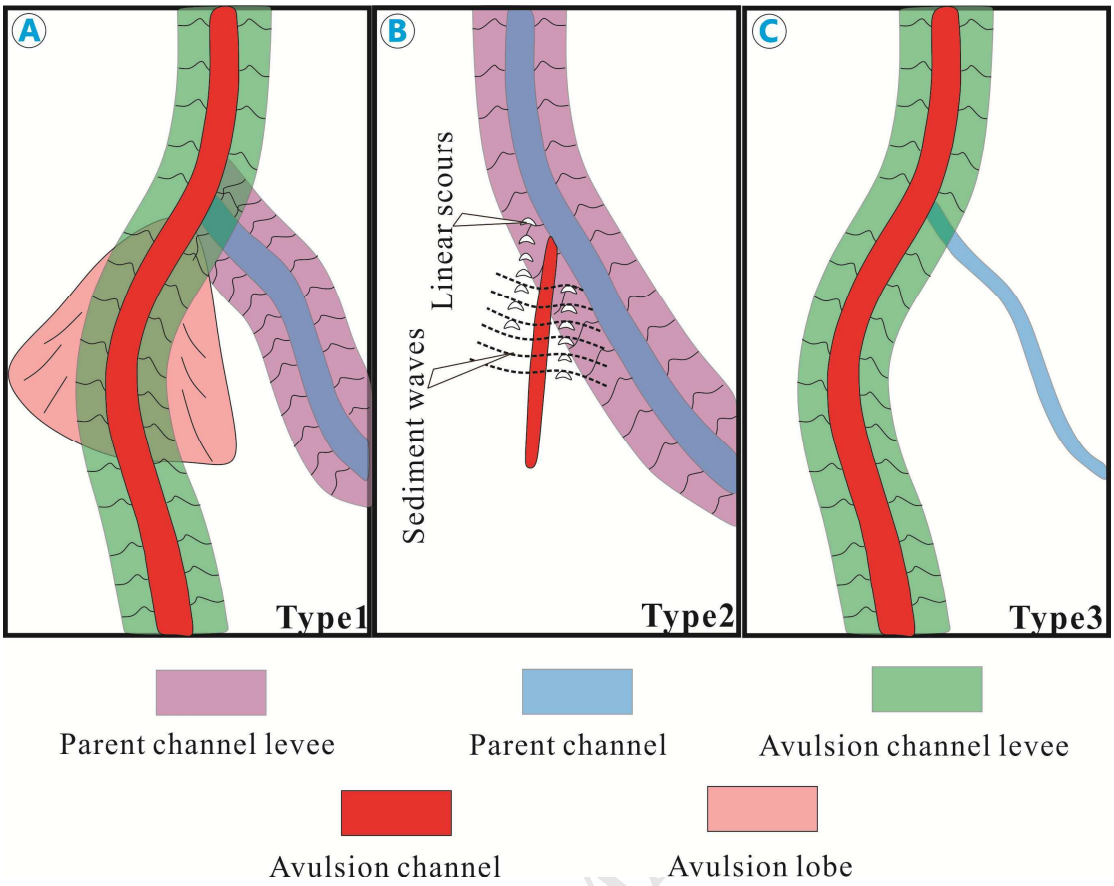

Fig. 13. Three end-member types of submarine channel avulsion. (A) Type 1: the parent channel and the avulsion channel have similar degrees of maturity and size and an avulsion lobe is commonly recognized at the base of the avulsion channel. (B) Type 2: large, high-maturity parent channel and small, low maturity avulsion channel; around the avulsion point sediment waves and linear scours (oriented perpendicular and parallel to the direction of the avulsed flows, respectively) are commonly observed. (C) Type 3: large and mature avulsion channel; around the avulsion point the head of the parent channel is overlain by the levee deposits of the avulsion channel.

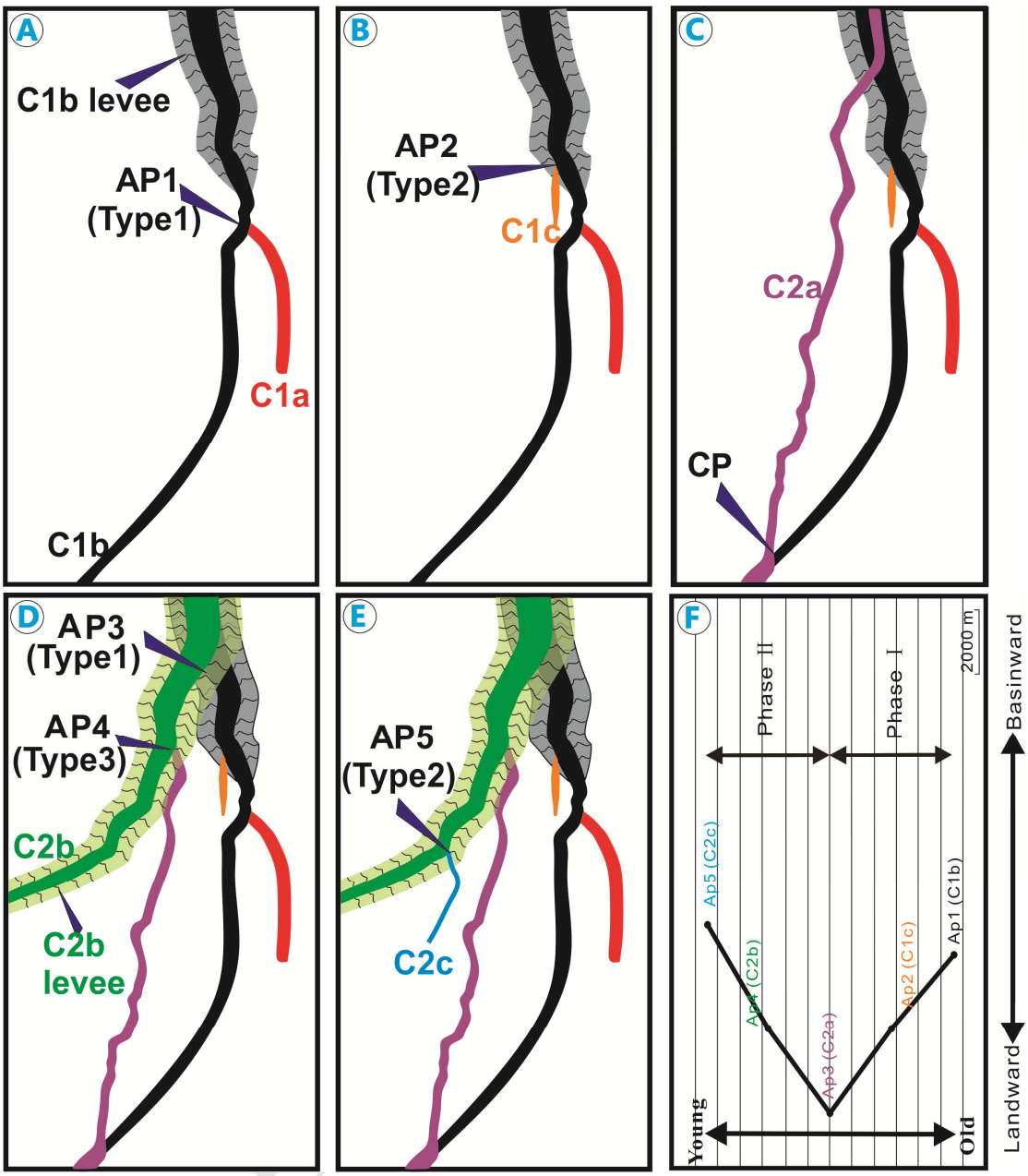

Fig. 14. Temporal-spatial evolution model of the ACS. (A-E) Diagrams showing C1a, C1b, C1c, C2a, C2b and C2c and associated AP1-AP5 came into being successively. The differences between parent channel and avulsion channel and the specific type of avulsion events are also shown in each panel. (F) Relative position along depositional dip and relative age of the five channel avulsions documented in the present study. Note that the avulsion points first back-stepped (i.e. moved toward the shelf) in Phase I and then fore-stepped (i.e. moved toward the basin) in Phase II. Because available data do not allow constraining the absolute age of the avulsions, the plot shows time intervals between avulsions as equal, just for display.

- A channel system consisting of six avulsion channels is analysed offshore Nigeria.
- MTC-related confinement controls the development of avulsion channels.
- Three ideal categories of submarine channel avulsions are observed.
- Topography related to mud diapirs provided lateral confinement to capture channel flows.